Article

Strong spectral features from asymptotic giant branch stars in distant quiescent galaxies

Shiying Lu [●][1,2,3] ✉, Emanuele Daddi [●][2] ✉, Claudia Maraston [●][4] ✉,
Mark Dickinson [●][5], Pablo Arrabal Haro [●][5], Raphael Gobat [●][6], Alvio Renzini[7],
Mauro Giavalisco[8], Micaela B. Bagley[9], Antonello Calabrò[10], Yingjie Cheng [●][8],
Alexander de la Vega[11], Chiara D'Eugenio[12,13], David Elbaz[2],
Steven L. Finkelstein [●][9], Carlos Gómez-Guijarro [●][2], Qiusheng Gu [●][1,3],
Nimish P. Hathi [●][14], Marc Huertas-Company[12,13,15], Jeyhan S. Kartaltepe [●][16],
Anton M. Koekemoer [●][14], Aurélien Henry[17], Yipeng Lyu[2], Benjamin Magnelli [●][2],
Bahram Mobasher[11], Casey Papovich [●][18,19], Nor Pirzkal [●][20], R. Michael Rich[21],
Sandro Tacchella [●][22,23] & L. Y. Aaron Yung [●][14]

Dating the ages and weighting the stellar populations in galaxies are essential steps when studying galaxy formation through cosmic times. Evolutionary population synthesis models with different input physics are used for this purpose. Moreover, the contribution from the thermally pulsing asymptotic giant branch (TP-AGB) stellar phase, which peaks for intermediate-age 0.6–2 Gyr systems, has been debated for decades. Here we report the detection of strong cool-star signatures in the rest-frame near-infrared spectra of three young (~1 Gyr), massive (~$10^{10}\,M_\odot$) quiescent galaxies at large look-back time, $z = 1$–2, using JWST/NIRSpec. The coexistence of oxygen- and carbon-type absorption features, spectral edges and features from rare species, such as vanadium and possibly zirconium, reveal a strong contribution from TP-AGB stars. Population synthesis models with a significant TP-AGB contribution reproduce the observations better than those with a weak TP-AGB, which are commonly used. These findings call for revisions of published stellar population fitting results, as they point to populations with lower masses and younger ages and have further implications for cosmic dust production and chemical enrichment. New generations of improved models are needed, informed by these and future observations.

The thermally pulsing asymptotic giant branch (TP-AGB)—an advanced evolutionary stage of low- and intermediate-mass stars (0.8–10 $M_\odot$)—is a potentially essential component of stellar population models. Quantifying the TP-AGB contribution to the light of stellar populations has a long history. The first estimate goes back over 30 years (ref. [1]) and was based on the fuel-consumption theorem[2]. It predicted that the TP-AGB contribution to the bolometric light of a simple stellar population (SSP) could approach or even exceed ~50% at intermediate ages.

Subsequent models estimated a contribution of up to ~80% of the integrated near-infrared (NIR) emission of stellar populations with ages in the range 0.2 ≲ t ≲ 2 Gyr (refs. [3–7]).

The actual energetic contribution and spectral composition of this phase, however, remain highly controversial, with different models adopting distinctively different prescriptions for both the energetics and the stellar spectra[4,8–10]. These uncertainties stem from two complications typical of the TP-AGB phase, namely its double-shell

burning regime, leading to instabilities and 'thermal pulses' on short timescales alongside a strong mass loss, both requiring the calibration of free parameters, such as convection, mixing and mass loss, with observations[11,12]. As a consequence, stellar evolutionary computations, which are the backbone of evolutionary population synthesis models, typically terminate at the end of the early AGB, and the inclusion of the TP-AGB in integrated models is performed separately, using either specific TP-AGB tracks[5,9] or TP-AGB energetics estimated by the fuel-consumption theorem[4].

Historically, the early Maraston (M05) models[4] based on the fuel-consumption theorem[2] pioneered the incorporation of the TP-AGB phase into population synthesis models by calibrating the energetics of TP-AGB tracks with observed photometric data and adopting observed oxygen-rich (O-rich) and carbon-rich (C-rich) spectra[13,14]. These M05 models, which forecast the onset of the TP-AGB phase as a sharp transition (for example, a rapid increase in the TP-AGB bolometric and NIR contribution to the energetics of stellar populations[3]) around 0.2 Gyr and lasting up to 2 Gyr, are referred to as 'TP-AGB-heavy'. A similar approach is found in the Conroy (C09) models[10], but with two modifications, namely that there is a substantial reduction of the energetics and a shift towards older ages (1–3 Gyr) for the relevant population epoch, which dilute the TP-AGB 'phase transition'. The C09 models are referred to as 'TP-AGB-light'. Following the availability of new data for the calibration and adopting some of the C09 arguments, the calibration of the TP-AGB contribution as a function of age was revised using data for globular clusters in the Magellanic Clouds[11]. These updated versions of the M05 models are the M13 models, which are referred to as 'TP-AGB-mild'. They have a reduced TP-AGB fuel consumption and a slightly older onset age (600 Myr) with respect to M05 but still predict a sharp transition for the TP-AGB onset and sizeable fuel consumption. Finally, the widely used Bruzual & Charlot (BC03) models[8], which are based on an isochrone synthesis of stellar evolutionary tracks[15], adopt different energetics and spectra for the TP-AGB phase. As this results in a negligible TP-AGB contribution to the integrated spectrum, the BC03 models are referred to as 'TP-AGB-poor'.

Many studies have attempted to observationally constrain the contribution of the TP-AGB phase by fitting spectra and photometric spectral energy distributions (SEDs) of different types of galaxies (post-starbursts, Seyferts, spirals and passive) over a range of redshifts, with conflicting results[16–19]. Quiescent high-redshift galaxies (mass-weighted ages of ~1 Gyr produce the peak contribution of TP-AGB stars to the NIR) are ideal laboratories but until now, imaging data have been available only at high redshift. High-quality NIR galaxy spectra dominated by TP-AGB stars are still missing: ground-based spectra below 2.3 μm are impacted by atmospheric emission and absorption, and NIR grism spectra from the Hubble Space Telescope (HST) lack sufficient sensitivity. The James Webb Space Telescope (JWST) now has the wavelength coverage and sensitivity to finally settle this issue.

Results
Selection of quiescent galaxies
We searched for distant quiescent galaxies serendipitously included (as fillers) in the Cosmic Evolution Early Release Science (CEERS) programme of the near-infrared spectrograph (NIRSpec) onboard JWST[20,21] and during a subsequent NIRSpec follow-up programme (DD-2750)[22]. We started by identifying 1,084 quiescent galaxy candidates at $z_{phot} > 1$ in the CANDELS extended Groth strip[23,24] catalogue[25], based on the UVJ diagram[26] and SED modelling (adopting an exponentially declining star-formation history, SFH $\propto e^{-t/\tau}$ and requiring $t/\tau > 1.0$), in which τ is the e-folding quenching timescale, and t is the time since the onset of star formation. The $z > 1$ limit ensures that the age-sensitive spectral region around the rest-frame 4,000 Å break is covered by JWST/NIRSpec with good sensitivity. We cross-matched these photometric candidates with the 1,491 galaxies already with a secure NIRSpec spectroscopic redshift. This resulted in 31 galaxies, whose spectra we visually
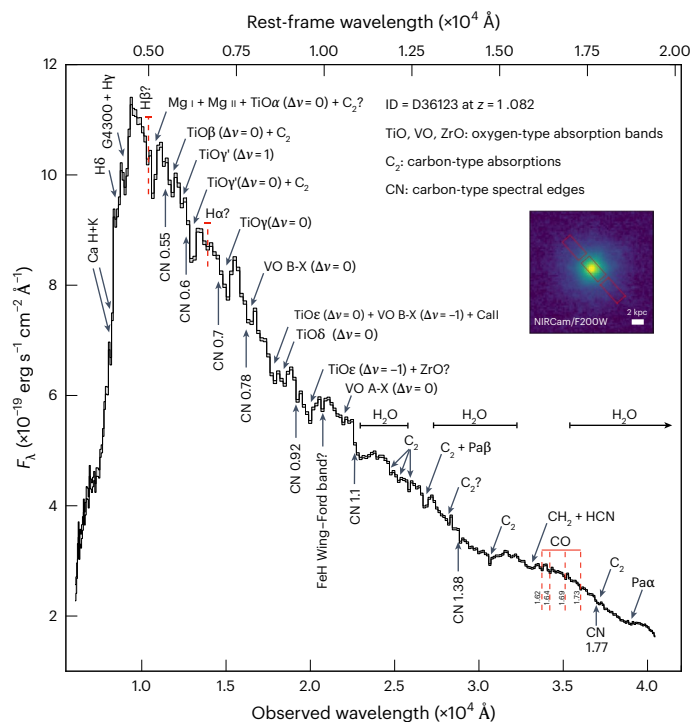

Fig. 1 | NIR rest-frame spectrum of the quiescent galaxy D36123 at z = 1.082. The upper and lower histograms (filled in grey) display the 1σ uncertainty range (notice the high SNR). The rest-frame wavelengths were calculated from the redshift corresponding to the best-fitting M13 models. Black arrows point to identifications of oxygen-type and carbon-type absorption and the detections of deep CN edges (see also Supplementary Table 1). Both sets of features are characteristic of carbon-rich and oxygen-rich stars in the TP-AGB phase. Question marks indicate uncertain features. Inset, NIRCam image in the F200W band together with the layout of the NIRSpec shutters (each shutter was 0.2'' × 0.46'').

inspected. Some spectra have a low signal-to-noise ratio (SNR) because the galaxies are faint or poorly centred in the NIRSpec's micro-shutter apertures. Other spectra had strong emission lines consistent with either active star formation or an active galactic nucleus. A few have redshifts ($z > 3$) that are too high to provide adequate coverage of the relevant rest-frame NIR wavelengths. We retained three galaxies, IDs 8595, 9025 and D36123, which have redshifts of $1 < z < 2$ and whose spectra clearly show the D4000 break and no obvious emission lines and have relatively high SNR.

The primary spectrum of galaxy D36123
Galaxy D36123 exhibits an exceptionally high-quality PRISM spectrum with an average of SNR ≥ 187 per spectral pixel (Fig. 1; plotted as a double histogram showing the ±1σ noise). The relatively bright flux (mag$_{AB}$ = 21.4 at 3.6 μm), steep radial surface brightness profile (Sérsic $n ≈ 4$; Extended Data Fig. 1), longer exposure time and accurate centring into the micro-shutters, which minimizes the effect of path loss and aperture correction (Methods), are the reasons for the notable quality of this spectrum.

A large number of features were clearly detected at rest-frame wavelengths from 0.3 to 2.0 μm, for which we propose identifications (see labels in Fig. 1 and Supplementary Table 1). Besides common absorption features at $\lambda_{rest} < 5,500$ Å typical of quiescent galaxies, such as Ca H+K, Hδ and Hγ+G4300, and absorption from heavy elements such as Mg, Ca and Fe, which have been observed in quiescent galaxies at high redshift[27], the spectrum exhibits numerous absorption features and band edges. The relatively low spectral resolution ($R ≈ 30–300$) of NIRSpec PRISM helped in the detection of these
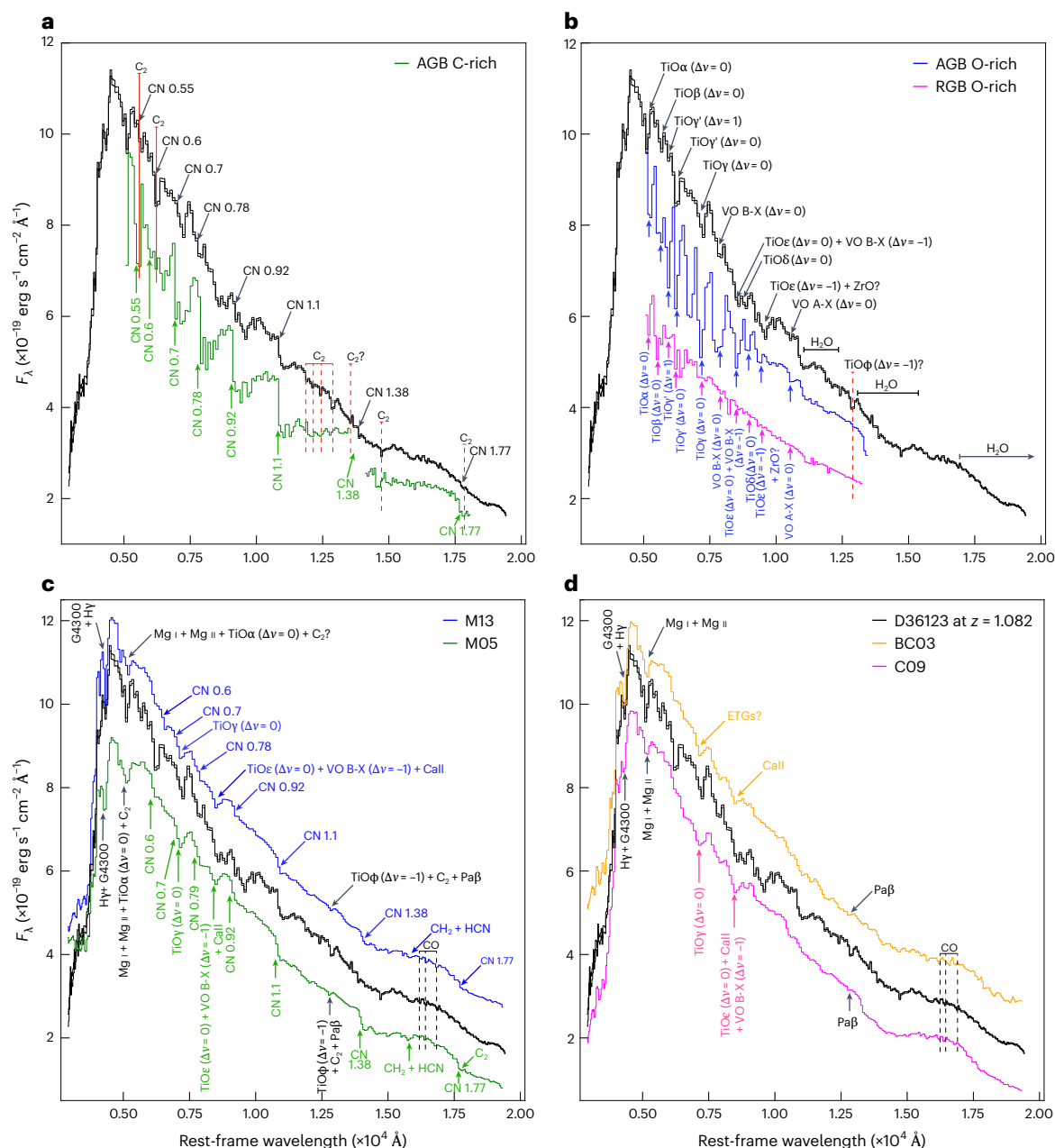
Fig. 2 | Identified features and best-fitting models for D36123. a,b, Identified TP-AGB features (solid arrows) based on Milky Way stars. **a,** The deep CN edges and carbon-containing molecules are confirmed by comparing them to a C-rich (C1) star[14] (green) in the TP-AGB phase. **b,** The TiO, VO and ZrO absorptions were identified as stemming from an O-rich star in the coldest bin[13] (blue) in the TP-AGB phase. The O-rich static giants[35] with $(I - K)_{colour}$ = 2.01 in the RGB phase are plotted in magenta, with dashed arrows indicating the positions of unmatched features. For clarity, the stellar spectra are stretched to follow the continuum shape of our high-redshift target. **c,d,** D36123 spectrum fitted with stellar population models. **c,** TP-AGB-mild (M13, blue) and TP-AGB-heavy (M05, green) models. **d,** TP-AGB-poor (BC03, orange) and TP-AGB-light (C09, magenta) models. The curve for each best-fitting model was shifted for clarity. Black arrows and labels highlight features identified by all four models at the same absorption positions. Two absorption features in orange (magenta) were identified by the BC03 (C09) model. Other CN edges and oxygen-type absorptions were identified by the M13 and M05 models. The black histograms in all panels show the rest-frame spectrum of D36123 and its errors, adopting the redshift z = 1.082 from the M13 best fit.

broad features. The proposed identifications were obtained by comparison with empirical libraries of C-rich[14] and O-rich[13] TP-AGB stars (Fig. 2a,b). These features are related to diverse stellar types in the AGB stellar phases, that is the early AGB and TP-AGB[28–31]. The deep CN edges in Fig. 2a (most striking is the CN 1.1 μm edge in Fig. 1, where the continuum suddenly dropped by ~15%) are particularly enhanced in N-type carbon stars[28–30], which are produced by the third dredge-up. These deep CN edges, therefore, demonstrate the presence of the contribution by TP-AGB stars (see the CN 1.1 index in Fig. 3d,f). On

the other hand, the TiO and VO absorption bands (Fig. 2b) are produced in cool M-type stars, in either the red giant branch (RGB) or AGB[29], but the equivalent width (EW) measured for specific features at 0.50–0.53 and 0.9–1.0 μm and the strength of the 1.6 μm H bump are all larger than what would be expected for the RGB alone, when diluted by the rest of the stellar phases, which are featureless at these wavelengths (Fig. 3e,f). Multiple TiO absorptions concomitant with CN and C_2 features have been observed in a galaxy's spectrum, pointing to the simultaneous presence of O-rich and C-rich cool stars. This
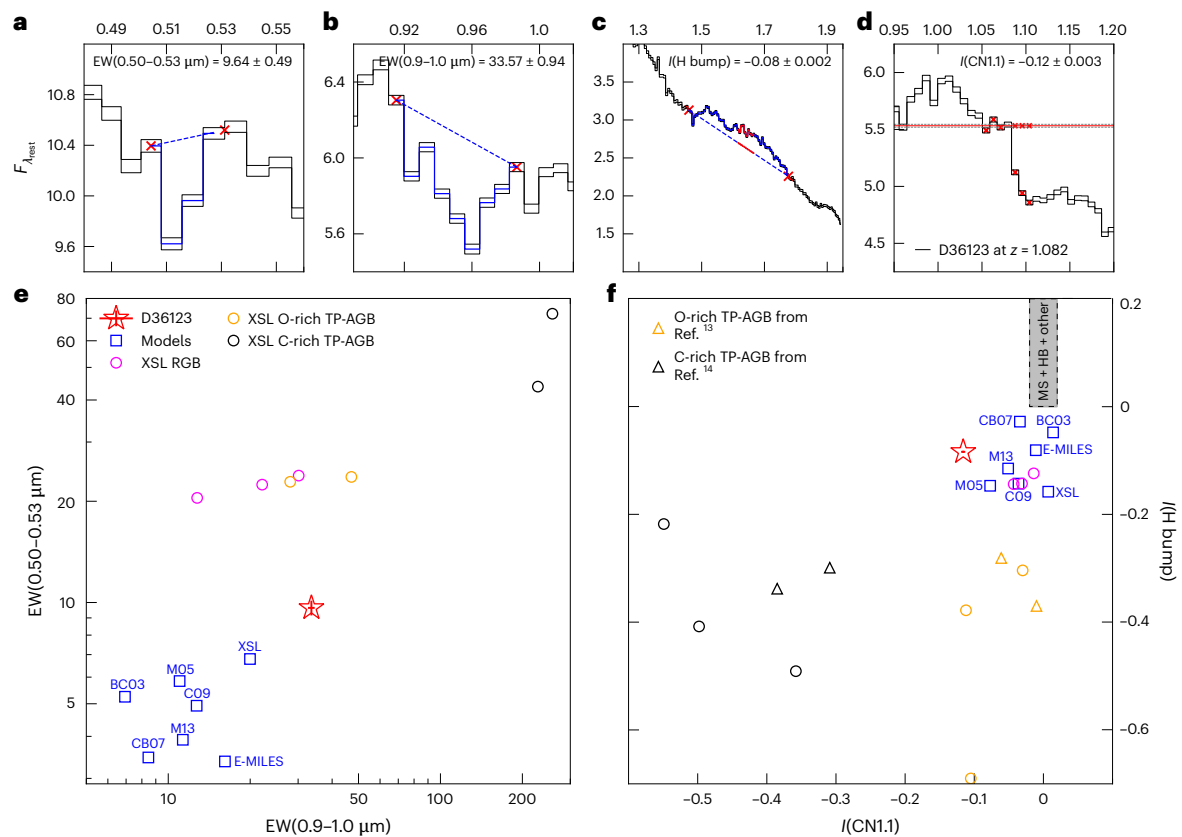
Fig. 3 | Specific features and comparison with models and stellar templates.
a–**d**, Specific features of galaxy D36123 in the rest frame. EW at 0.50–0.53 μm (**a**)
and 0.9–1.0 μm (**b**). Strength of the H-band bump at -1.6 μm (**c**) and of the CN1.1
edge at -1.1 μm (**d**). **e**,**f**, Comparisons of the best-fitting models and cool stars.
e, Relation between EW(0.50–0.53 μm) and EW(0.9–1.0 μm). **f**, Relation between
two indices, I(H bump) and I(CN1.1). Values for the indices for models and cool

stars are listed in Extended Data Table 1. Cool stars include the O-rich static giants
(RGB) and C- and O-rich TP-AGB stars from the averaged spectra of XSL[35], shown
by circles in **e**. Other C- or O-rich TP-AGB stars from other libraries[13,14] are shown
by triangles in **f**. The grey shaded area in **f** shows the distribution of the main
sequence (MS), horizontal branch (HB), and others during the stellar phases.

was naturally expected for a broad distribution of stellar metallicities,
which must exist in massive galaxies, such that the metal-poor stars
evolve preferentially into C-rich TP-AGB stars and the metal-rich
ones into O-rich (M-type) TP-AGB stars[2]. As V and Zr are produced by
only s-process nucleosynthesis, those VO and ZrO features (Fig. 2b),
indicative of a recent third dredge-up episode, are expected only in
the coolest TP-AGB stars[29,31], demonstrating the prominence of the
TP-AGB phase in the light emitted by this $z \approx 1$ quiescent galaxy.

We subsequently fitted the spectrum of D36123, employing four
models: BC03, C09, M13 and M05. These span the full range from
TP-AGB poor to heavy (Fig. 2c,d and Table 1). The first two models are
the standard for deriving the physical properties of high-redshift galax-
ies. We used a delayed exponentially declining SFH $\propto (t/\tau^2)e^{-t/\tau}$ with a
large variety of timescales and stellar ages, interpolated over a grid of
metallicities, and allowed for dust extinction. When convolving the
models to match the resolution of observed spectra, we considered
the instrumental resolution, the wavelength sampling of the spectral
template models and the estimated stellar velocity dispersion of the
galaxy (Methods). We found that our model fitting results were robust
against (1) more complex SFHs allowing for bursts and sudden trunca-
tions, (2) a non-parametric SFH obtained as linear combinations of
models with different ages and metallicities, (3) alternative attenuation
curves or without considering the reddening by dust, (4) variations to
the aperture-correction recipe, (5) modifications of the spectral extrac-
tion apertures over 3 or 5 pixels and (6) modelling of emission lines.
The minimum reduced χ_R^2 from each model was barely affected when
these variations are considered.

The TP-AGB-mild and -heavy models (M13 and M05) can repro-
duce the largest fraction of the detected features, whereas the
TP-AGB-poor and -light models predict much weaker spectral features
in the NIR, as Figs. 2c,d and 3e,f illustrate (also Extended Data Table 1).
The TP-AGB-mild model, M13, provided the best overall fit and also
identified most of the TP-AGB features (four TiO absorptions and most
CN edges). However, even in the M13 best-fitting spectrum, some
strong spectral features are clearly not present (or much weaker than
in the observed spectrum), like several TiO and C_2 absorptions. The
strong CN1.1 μm spectral edge is best reproduced by the M13 and M05
models (Fig. 3f). Interestingly, the Mg II band at 0.52 μm, one of the
Lick indices[32], is much weaker in all models than in the data (Fig. 3e),
pointing to a strong contribution from TiO bands all the way to 0.5 μm,
as expected for M-type stars (and, possibly, to [α/Fe] enhancement[33]).
Overall, M05 produced the worst fit due to a clear discrepancy at
$\lambda_{rest} < 5,000$ Å (Extended Data Fig. 2) but still had significantly more
matching TP-AGB features in the NIR than the C09 and BC03 models
(Fig. 2c,d), noticeably the long-sought C_2 absorption around 1.75 μm.
Moreover, when fitting the spectrum over the restricted range
$\lambda_{rest} < 5,000$ Å, all models converged to a mass-weighted age of about
1 Gyr, which is, indeed, the age when TP-AGB features are expected to
nearly peak[4,11]. Therefore, we conclude that the treatment of the
TP-AGB in the models most affects the goodness of fit in our $z \approx 1$
quiescent galaxies. Even for the top-performing model, M13, the
minimum reduced $\chi_R^2 \approx 39$ was large, indicating that this model also
lacks stellar ingredients that are present in the galaxy and are
necessary.

Table 1 | Stellar population properties of D36123

Rest-frame spectral range	Property	BC03 TP-AGB-poor	C09 TP-AGB-light	M13 TP-AGB-mild	M05 TP-AGB-heavy
		Right ascension (RA) 14 h 19 m 34.258 s		Declination (dec.) +52°56′23.079″	
Full (0.3–2.0 μm)	Redshift	$1.074^{+0.001}_{-0.001}$	$1.075^{+0.003}_{-0.001}$	$1.082^{+0.002}_{-0.002}$	$1.075^{+0.002}_{-0.004}$
	M_* ($\times10^{10}\,M_\odot$)	$1.493^{+0.007}_{-0.004}$	$1.489^{+0.007}_{-0.006}$	$1.167^{+0.008}_{-0.005}$	$1.552^{+0.015}_{-0.014}$
	Age (Gyr)	$1.661^{+0.024}_{-0.041}$	$0.751^{+0.025}_{-0.034}$	$0.621^{+0.029}_{-0.021}$	$2.224^{+0.016}_{-0.024}$
	$Z/Z_\odot$	$1.944^{+0.028}_{-0.034}$	$2.000^{+0.000}_{-0.008}$	$1.589^{+0.061}_{-0.039}$	$0.982^{+0.001}_{-0.001}$
	Av	$0.000^{+0.002}_{-0.000}$	$0.156^{+0.016}_{-0.022}$	$0.424^{+0.026}_{-0.026}$	$0.000^{+0.000}_{-0.000}$
	τ (Gyr)	$0.241^{+0.019}_{-0.018}$	$0.104^{+0.014}_{-0.021}$	$0.100^{+0.010}_{-0.010}$	$0.707^{+0.013}_{-0.017}$
	SFR$_{best}$ ($M_\odot\,yr^{-1}$)	$0.294^{+0.036}_{-0.065}$	$0.099^{+0.001}_{-0.001}$	$0.311^{+0.003}_{-0.003}$	$1.320^{+0.006}_{-0.006}$
	SFR$_{best}$/SFR$_{peak}$	$0.019^{+0.011}_{-0.010}$	$0.014^{+0.022}_{-0.015}$	$0.024^{+0.024}_{-0.023}$	$0.368^{+0.032}_{-0.024}$
	χ^2_R	59.6	52.9	39.0	102.6
Optical (<0.5 μm)	Redshift	$1.078^{+0.002}_{-0.002}$	$1.083^{+0.001}_{-0.002}$	$1.078^{+0.001}_{-0.002}$	$1.078^{+0.001}_{-0.002}$
	M_* ($\times10^{10}\,M_\odot$)	$1.330^{+0.019}_{-0.013}$	$1.406^{+0.033}_{-0.043}$	$1.140^{+0.011}_{-0.197}$	$1.151^{+0.024}_{-0.021}$
	Age (Gyr)	$0.961^{+0.021}_{-0.026}$	$0.810^{+0.005}_{-0.003}$	$0.909^{+0.098}_{-0.098}$	$0.969^{+0.031}_{-0.069}$
	$Z/Z_\odot$	$1.525^{+0.095}_{-0.225}$	$2.000^{+0.000}_{-0.007}$	$2.183^{+0.017}_{-0.041}$	$1.002^{+0.048}_{-0.052}$
	Av	$0.068^{+0.082}_{-0.068}$	$0.000^{+0.034}_{-0.000}$	$0.000^{+0.038}_{-0.000}$	$0.000^{+0.002}_{-0.000}$
	τ (Gyr)	$0.007^{+0.017}_{-0.006}$	$0.091^{+0.025}_{-0.026}$	$0.001^{+0.010}_{-0.000}$	$0.007^{+0.043}_{-0.000}$
	SFR$_{best}$ ($M_\odot\,yr^{-1}$)	$0.000^{+0.004}_{-0.000}$	$0.093^{+0.001}_{-0.001}$	$0.000^{+0.006}_{-0.000}$	$0.000^{+0.010}_{-0.000}$
	SFR$_{best}$/SFR$_{peak}$	~0	~0	~0	~0
	χ^2_R	11.4	9.0	11.2	11.2
NIR (>0.5 μm)	Redshift	$1.074^{+0.001}_{-0.001}$	$1.080^{+0.002}_{-0.004}$	$1.083^{+0.002}_{-0.002}$	$1.080^{+0.003}_{-0.001}$
	M_* ($\times10^{10}\,M_\odot$)	$1.679^{+0.023}_{-0.031}$	$1.514^{+0.028}_{-0.021}$	$1.247^{+0.038}_{-0.017}$	$0.556^{+0.010}_{-0.004}$
	Age (Gyr)	$1.961^{+0.011}_{-0.039}$	$0.783^{+0.031}_{-0.028}$	$0.490^{+0.041}_{-0.041}$	$0.207^{+0.014}_{-0.009}$
	$Z/Z_\odot$	$1.883^{+0.040}_{-0.034}$	$2.000^{+0.000}_{-0.016}$	$0.692^{+0.029}_{-0.032}$	$0.500^{+0.022}_{-0.000}$
	Av	$0.000^{+0.006}_{-0.000}$	$0.103^{+0.022}_{-0.022}$	$0.706^{+0.049}_{-0.044}$	$0.982^{+0.029}_{-0.012}$
	τ (Gyr)	$0.497^{+0.029}_{-0.032}$	$0.057^{+0.016}_{-0.017}$	$0.023^{+0.010}_{-0.010}$	$2.605^{+0.332}_{-0.316}$
	SFR$_{best}$ ($M_\odot\,yr^{-1}$)	$0.984^{+0.177}_{-0.148}$	$0.000^{+0.012}_{-0.000}$	$0.000^{+0.018}_{-0.000}$	$23.725^{+0.013}_{-0.104}$
	SFR$_{best}$/SFR$_{peak}$	$0.207^{+0.057}_{-0.049}$	~0	~0	$0.200^{+0.029}_{-0.024}$
	χ^2_R	60.7	58.5	40.7	66.6
Full (excluding 0.5–1.0 μm)	Redshift	$1.076^{+0.001}_{-0.001}$	$1.093^{+0.001}_{-0.002}$	$1.081^{+0.001}_{-0.001}$	$1.075^{+0.002}_{-0.003}$
	M_* ($\times10^{10}\,M_\odot$)	$1.581^{+0.015}_{-0.014}$	$1.750^{+0.087}_{-0.002}$	$1.076^{+0.008}_{-0.002}$	$1.535^{+0.021}_{-0.025}$
	Age (Gyr)	$1.627^{+0.021}_{-0.019}$	$1.446^{+0.095}_{-0.046}$	$0.712^{+0.018}_{-0.012}$	$2.183^{+0.038}_{-0.040}$
	$Z/Z_\odot$	$2.300^{+0.048}_{-0.036}$	$0.300^{+0.010}_{-0.009}$	$1.285^{+0.030}_{-0.023}$	$0.990^{+0.007}_{-0.007}$
	Av	$0.000^{+0.004}_{-0.000}$	$0.078^{+0.023}_{-0.017}$	$0.068^{+0.014}_{-0.013}$	$0.000^{+0.009}_{-0.000}$
	τ (Gyr)	$0.028^{+0.012}_{-0.008}$	$0.127^{+0.054}_{-0.065}$	$0.095^{+0.009}_{-0.010}$	$0.690^{+0.012}_{-0.014}$
	SFR$_{best}$ ($M_\odot\,yr^{-1}$)	$0.000^{+0.008}_{-0.000}$	$0.000^{+0.045}_{-0.000}$	$0.084^{+0.013}_{-0.012}$	$1.306^{+0.022}_{-0.010}$
	SFR$_{best}$/SFR$_{peak}$	~0	~0	$0.011^{+0.009}_{-0.008}$	$0.363^{+0.027}_{-0.022}$
	χ^2_R	32.2	23.1	16.3	83.7
	$\chi^2_{R,\,msk}$	446.7	308.4	157.9	172.1

The first column denotes the rest-frame range of the wavelength adopted in the spectral fit. The third to sixth columns list the best-fitting physical properties derived by four models with different TP-AGB treatments. Specifically, the total stellar masses were based on the Chabrier IMF[66]. The age is the mass-weighted age, that is, the average over the look-back time weighted by the SFH. The best-fitting parameters and errors were derived from the distribution of χ^2, with the former obtained for the minimum χ^2. The errors were determined after rescaling to $\chi^2_R = 1$. SFR$_{best}$/SFR$_{peak}$ is a measure of quiescence, where SFR$_{best}$ was derived from the best fit by adopting delay-τ models, and SFR$_{peak}$ corresponds to the SFR maximum at $t = \tau$. $\chi^2_{R,\,msk}$ presents the reduced χ^2 within the masked 0.5–1.0 μm region during the spectral fit.
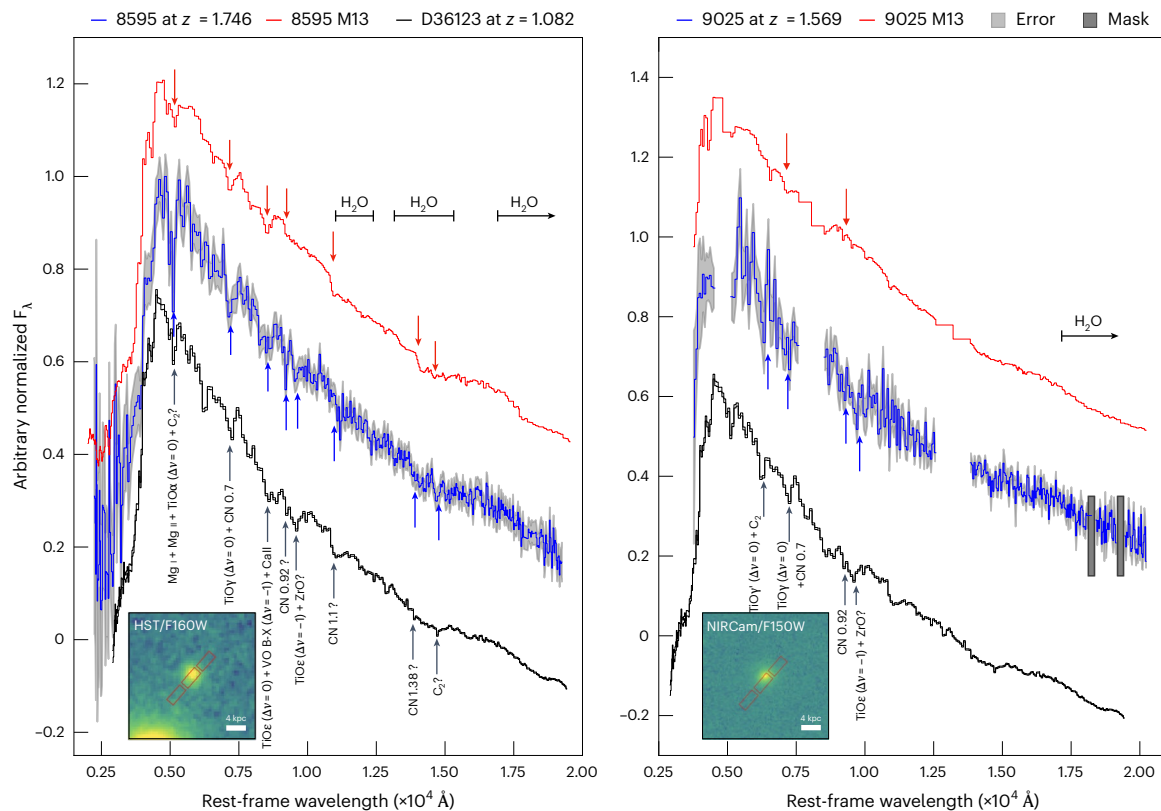
Fig. 4 | NIR spectra and identified features for the other two galaxies. The left and right panels are for galaxies 8595 and 9025, respectively. The observed spectra (blue) with errors (grey-shaded region) are compared with the M13 best-fitting models (red) and the spectrum of the bright galaxy D36123 (black) to identify features. The comparison spectra are shifted up or down for clarity. Blue arrows indicate matched features (labelled) in the spectra. Most features predicted by the M13 model are indicated by red arrows. Tentative identifications are shown with a question mark. Insets, HST/F160W (NIRCam/F150W) image for galaxy 8595 (9025), with NIRSpec shutters overlaid. Note that the observed spectrum of galaxy 9025 with the median resolution has been resampled to the PRISM spectral pixel grid to increase the SNR and for clarity. Some contaminated regions are blanked in the redder part of the spectrum of galaxy 9025. Detector defects in the spectrum of object 9025 are masked (grey rectangles; $\lambda_{rest} \approx 1.81$–$1.84\,\mu m$ and 1.92–$1.94\,\mu m$).

As mentioned, some observed features were also found in the coolest phase of (M-type) RGB stars (Fig. 2b) and the red supergiant phase of massive stars, which have ages around 10 Myr (refs. 13,28,31). We found that red supergiant stars did not contribute substantially due to the inferred mass-weighted age (~1 Gyr) and negligible residual star-formation rate (SFR) when we fitted only the optical spectrum (Table 1), implying a negligible contribution from short-lived massive stars. M-type RGB stars, on the other hand, certainly contribute to the NIR spectrum at these ages, to a degree that is, however, model-dependent because the onset and development of the RGB phase depends on the overshooting assumed in stellar tracks[4,34]. The full RGB contribution to the total light in the K band around 1 Gyr is ~20–30% according to M05 models and ~10–20% for BC03-type models. The upper part of the RGB where M-giants form is a further fraction of this. Therefore, although they contribute, M-type RGB stars are not expected to dominate the spectrum. This expectation is confirmed quantitatively by the measured indices in Fig. 3f, whose strengths are comparable to or even larger than those for individual RGB stars, which are necessarily diluted by the composite populations in galaxies. Therefore, many TP-AGB stars with strong features are needed to match the observed strengths of the features in the galaxy.

The best-fitting physical parameters presented in Table 1 exemplify the impact of the chosen model on the derived galaxy properties. For instance, comparing results between BC03 and M13 in the full rest-frame spectral range, there is only a 30% discrepancy in stellar mass, but the impact on ages is strong, with a stellar age difference $\Delta t \approx 1$ Gyr (the M13 age is almost three times shorter than the BC03

age), despite the higher metallicity preferred by the BC03 fit. These age differences affect the derived formation epochs and evolutionary timescales of galaxies.

We also fitted some other models. Two were entirely based on empirical stellar libraries (X-shooter Spectral Library (XSL)[35] and E-MILES[36]; see Extended Data Fig. 3a,b and Extended Data Table 2), but there were no significant improvements in the quality of fit or the reproduction of features (Fig. 3e,f). These models returned old ages >1.5 Gyr, with a subsolar metallicity best fit for E-MILES. The EW indices for XSL are closer to what was observed for D36123, but the model performed less well on CN 1.1 μm. The CB07 models (an updated version of BC03; Methods) behaved like M05 in providing a worse global fit but better match to specific deep features (for example, TiOγ at 0.73 μm; Extended Data Fig. 3c).

The spectra of galaxies 8595 and 9025
The spectra of the other two fainter quiescent galaxies, 8595 ($mag_{AB} = 24$ at 3.6 μm, observed with PRISM) and 9025 ($mag_{AB} = 23$ at 3.6 μm, observed with the medium-resolution gratings but rebinned to the PRISM resolution), have substantially lower SNR, ~15 and 7. Nevertheless, the SNRs is still sufficient to detect individual absorption features in object 8595 (Fig. 4, left). Some of the strongest features were observed for object 9025 (Fig. 4, right), including TiO absorption lines, CN spectral edges and, tentatively, a C_2 absorption feature.

Table 2 presents the results of the spectral fitting of objects 8595 and 9025. For object 8595, we carefully accounted for a neighbouring bright galaxy when measuring its photometry to estimate spectral

Table 2 | Stellar population properties of galaxies 8595 and 9025

Target (rest-frame)	Property	BC03 TP-AGB-poor	C09 TP-AGB-light	M13 TP-AGB-mild	M05 TP-AGB-heavy
8595 (full)		RA 14 h 20 m 42.240 s		Dec. +53° 01′ 50.298″	
	Redshift	$1.739^{+0.004}_{-0.002}$	$1.746^{+0.002}_{-0.003}$	$1.746^{+0.002}_{-0.003}$	$1.741^{+0.002}_{-0.002}$
	M_* ($\times 10^{10} M_\odot$)	$0.791^{+0.020}_{-0.020}$	$0.736^{+0.009}_{-0.007}$	$0.545^{+0.003}_{-0.003}$	$0.676^{+0.009}_{-0.009}$
	Age (Gyr)	$1.913^{+0.052}_{-0.052}$	$0.798^{+0.023}_{-0.023}$	$0.732^{+0.028}_{-0.027}$	$1.908^{+0.057}_{-0.058}$
	$Z/Z_\odot$	$1.711^{+0.039}_{-0.039}$	$2.000^{+0.000}_{-0.006}$	$1.584^{+0.044}_{-0.046}$	$1.878^{+0.012}_{-0.012}$
	Av	$0.012^{+0.051}_{-0.012}$	$0.357^{+0.023}_{-0.030}$	$0.368^{+0.020}_{-0.021}$	$0.013^{+0.022}_{-0.013}$
	τ (Gyr)	$0.283^{+0.029}_{-0.034}$	$0.134^{+0.041}_{-0.048}$	$0.133^{+0.038}_{-0.055}$	$0.403^{+0.022}_{-0.025}$
	SFR_{best} ($M_\odot$ yr^{-1})	$0.073^{+0.015}_{-0.015}$	$0.049^{+0.004}_{-0.004}$	$0.061^{+0.004}_{-0.004}$	$0.232^{+0.019}_{-0.018}$
	SFR_{best}/SFR_{peak}	$0.021^{+0.018}_{-0.015}$	$0.042^{+0.078}_{-0.078}$	$0.061^{+0.142}_{-0.098}$	$0.113^{+0.038}_{-0.034}$
	χ^2_R	0.821	0.950	0.794	0.935
	$P(\Delta\chi^2)$	0.00103	0	–	0
9025 (full+HST)		RA 14 h 19 m 33.991 s		Dec. +52° 51′ 56.290″	
	Redshift	$1.545^{+0.001}_{-0.001}$	$1.546^{+0.001}_{-0.002}$	$1.569^{+0.001}_{-0.002}$	$1.569^{+0.001}_{-0.002}$
	M_* ($\times 10^{10} M_\odot$)	$0.759^{+0.082}_{-0.046}$	$0.859^{+0.087}_{-0.042}$	$0.755^{+0.052}_{-0.050}$	$0.746^{+0.025}_{-0.023}$
	Age (Gyr)	$1.560^{+0.073}_{-0.122}$	$1.580^{+0.065}_{-0.062}$	$0.272^{+0.045}_{-0.045}$	$0.182^{+0.001}_{-0.018}$
	$Z/Z_\odot$	$2.123^{+0.203}_{-0.075}$	$0.300^{+0.004}_{-0.003}$	$1.700^{+0.115}_{-0.124}$	$1.140^{+0.064}_{-0.045}$
	Av	$0.351^{+0.061}_{-0.103}$	$0.397^{+0.026}_{-0.025}$	$1.125^{+0.048}_{-0.042}$	$1.337^{+0.052}_{-0.046}$
	τ (Gyr)	$0.304^{+0.037}_{-0.042}$	$0.316^{+0.063}_{-0.071}$	$0.019^{+0.008}_{-0.010}$	$0.008^{+0.006}_{-0.007}$
	SFR_{best} ($M_\odot$ yr^{-1})	$0.181^{+0.024}_{-0.013}$	$0.230^{+0.045}_{-0.028}$	$0.048^{+0.014}_{-0.014}$	$0.027^{+0.004}_{-0.004}$
	SFR_{best}/SFR_{peak}	$0.082^{+0.068}_{-0.056}$	$0.092^{+0.107}_{-0.095}$	~0	~0
	χ^2_R	1.702	1.838	1.634	1.649
	$P(\Delta\chi^2)$	0.00001	0	–	0.03767

For both objects, the spectral fit used the entire rest-frame wavelength range. Additionally, to better constrain the age-sensitive wavelength around 4,000 Å, two other HST bands (F606W+F814W) were employed simultaneously in the fit of object 9025 (Methods). Measurements and errors are as in Table 1, except that we did not rescale the reduced χ^2 to 1. $\Delta\chi^2$ was computed relative to the M13 model.

aperture corrections, following a similar approach to what was done for object D36123 (Methods). Again, M13 yielded the best-fitting spectral fits for both galaxies, with $\chi^2_R \approx 0.9$ for object 8595 and $\chi^2_R \approx 1.7$ for object 9025. The derived stellar masses differ at most by 0.16 dex between the M13 and BC03 models, but the best-fitting ages were even more strongly dependent on the specific model used ($\Delta t \approx 0.1$–1 Gyr). In Table 2, the values $\Delta\chi^2$ denote the χ^2 difference with respect to the M13 model. The small cumulative probability $P(\Delta\chi^2)$ suggests the preference for the M13 model is statistically significant in the overall spectral fitting for these two galaxies.

Discussion
Overall, we conclude that the spectra of the distant quiescent galaxies studied here show clear evidence of substantial contributions from both C- and M-type TP-AGB stars. The models with significant TP-AGB contributions, such as M13 and M05, are in better agreement with NIR features in the galaxies' spectra, whereas TP-AGB-mild models (M13) fit the full spectra better, supporting our conclusion that the TP-AGB is the primary model ingredient driving the quality of the fits.

Previous work[18] based on the NIR spectra of local spiral and Seyfert galaxies reached similar conclusions, favouring M05 models over BC03 models because of the TP-AGB component. Those local spectra cover a wide wavelength range like our high-redshift data and display various features, several of which can be attributed only to TP-AGB stars. Previously, detection of the CN 1.1 μm band in the NIR spectra of local active galactic nuclei has been interpreted as a signature of intermediate-age

populations evolving along the TP-AGB phase[30]. Although these local observations are notable, JWST spectroscopy can observe massive galaxies at high redshift. Their low spread in stellar generations allows for their stars to evolve through the TP-AGB phase in sync at age ~1 Gyr, when the TP-AGB energetic contribution is maximum[4,6]. This maximizes the contribution of the short TP-AGB phase (~3 Myr for an individual star) to the integrated galaxy SED, with respect to systems with continuing star formation and a lower mass fraction of stars in the appropriate age range.

Indeed, we found that even for the best-performing M13 model, χ^2_R was large for the high-SNR spectrum of D36123, which has stronger absorption features than the model. By separating optical data ($\lambda_{rest} < 0.5$ μm) from NIR data ($\lambda_{rest} > 0.5$ μm), we confirmed that the fit in the NIR spectrum leads to high values of χ^2, as we found a minimum reduced $\chi^2_R \approx 9$–11 in the optical spectrum for the four different models (C09 performed best in this case), whereas the reduced χ^2_R remained large ($\chi^2_R \approx 40$–60) when fitting only the NIR spectrum (Table 1). Interestingly, excluding from the fit the range $\lambda_{rest} = 0.5$–1.0 μm, which contains the strongest TiO features, the M13 and M05 models largely perform better than the other models when reproducing solely this region, pointing to a more consistent treatment of this spectral range, which is heavily affected by TP-AGB stars (Extended Data Fig. 2).

In any case, overall, χ^2_R was always large for each model and spectral range, suggesting that improvements to the models are necessary. Focusing on the best-fitting models, M13 (like M05) uses empirical spectra for just the TP-AGB phase. For the other phases contributing

to the NIR, such as the RGB, classical Kurucz-type theoretical spectra from model atmospheres are adopted, which—as is well known—do not adequately match all NIR absorption features[37,38]. On the other hand, models based on the empirical RGB spectra perform better, but not for all features[37], as we also show here. Notably, various studies have shown that all CO NIR spectral features from H to K in local massive early-type galaxies (ETGs), whose NIR spectra are dominated by RGB stars, are systematically stronger than those in models based on empirical libraries[39]. This is also observed in the NIR spectra of local spirals and star-forming galaxies[40]. This evidence suggests that D36123 also contains stars that are more metal-rich than those included in the model. Moreover, the M13 models apply local samples of C-rich and O-rich spectra, which may not cover the range of metallicity and abundance ratios hosted in distant massive ellipticals. The metallicity dependence of the relative contributions of C-rich and O-rich TP-AGB stars in M13 models is included using a theoretical prescription[2], such that in more metal-rich models, more fuel is consumed in O-rich rather than in C-rich phases, but they still use the same observed spectra. Moreover, the calibration of stellar population models requires samples of stellar generations that are as simple as possible, that is, star clusters, with independent age and chemical composition available from fitting a colour–magnitude diagram and from stellar spectroscopy. For the TP-AGB phase, these calibrating clusters also need to span a wide age range, extending down to ~100 Myr. Star clusters with these properties exist in the Magellanic Clouds and have traditionally served to calibrate stellar population models[3,11,41]. The limitation is that these clusters have subsolar metallicity and possibly solar or subsolar element ratios.

Another issue occurs when there is a galaxy-specific chemical pattern. It is well known that massive galaxies, both locally[33] as well as at high redshift[27,42], feature [α/Fe]-enhanced stellar populations. The same galaxies also have enhanced ratios of [C/Fe] and [N/Fe] (refs. [43,44]) and possibly also have Na (ref. [45,46]). Empirical libraries based on local, solar-scaled RGB spectra and the population models based on them may not reflect these chemical patterns, causing discrepancies. This mirrors a long-standing discrepancy between optical spectral features of massive galaxies and early population models[47], which was solved by using [α/Fe]-enhanced population models[48]. Galaxy spectra like those we present here, with young ages, supersolar metallicity and possibly various non-solar element enhancements, are unique, with unknown counterpart in the Universe. They challenge the models but also offer the invaluable opportunity to calibrate them, with far-reaching benefit also for stellar evolution and model atmosphere theories.

Inferring the timeline of galaxy evolution depends on population synthesis models. In turn, the model age scale depends on the input stellar evolution in terms of stellar tracks (and their input) and the energetics of stellar phases. We derive systematically younger ages and lower masses when fitting these spectra with TP-AGB-mild models (M13) versus TP-AGB-poor/-light models (BC03/C09), especially at high redshift. The age differences range from ~100 Myr to ~1 Gyr (Tables 1 and 2). Younger galaxy ages can have implications for the inferred physics of galaxy evolution, such as gas accretion and star-formation quenching. Also, galaxy simulations adopt evolutionary population synthesis models as input, hence our results impact the predicted spectra and photometry of simulated galaxies found in cosmological and other simulations[7]. In that case, the age was fixed within the simulation, but the simulated SEDs of the galaxies and the calibrations through comparisons to observations were obviously affected. The AGB stellar phase also has a large impact on galaxies' dust production and chemical evolution, particularly for heavy elements[49]. More fuel for this phase, as supported by our findings, has implications on the relevant calculations for these processes[50], thus potentially having an even broader impact on galaxy evolution.

The spectra presented here demonstrate the presence of TP-AGB spectral features, including those from carbon stars, in the integrated

NIR light of high-redshift quiescent galaxies. We have observed these features in all their complexity in galaxy spectra. Clearly, our very small galaxy sample does not allow us to infer, statistically, the impact of the TP-AGB emission on the derived stellar population properties of young quiescent galaxies. Previous photometric studies[6,19] have shown that, on average, fitting distant galaxies using models with heavier TP-AGB contributions yields younger ages and lower stellar masses than TP-AGB-poor models, but with significant galaxy-by-galaxy differences. The usual degeneracies among age, reddening and metallicity still apply to some extent and, for individual galaxies, the fitting results for the SEDs can depend on unknown details of the past SFHs (for example). From our small sample, evaluating how frequently these TP-AGB features are present in early galaxy spectra is also difficult. NIRSpec observations of a larger, homogeneously selected sample of galaxies as luminous as D36123 (which are common, even over a single NIRSpec pointing) could address these questions and help us to quantify the broader consequences of TP-AGB emission in determining galaxies' physical parameters. Such observations may also help to guide improvements to stellar population models.

Methods
NIRSpec observation and reduction
In this study, we present NIR spectra for three quiescent galaxies, IDs D36123, 8595 and 9025. We cross-matched the catalogue of the CANDELS extended Groth strip field[25] with the NIRSpec detections in the DD-ERS-1345 programme (CEERS, PI S. Finkelstein) and the DD-2075 programme (principal investigator P. Arrabal Haro). Both D36123 and 8595 were observed with PRISM[51], spanning 0.60–5.30 μm with various spectral resolutions $R \equiv \lambda/\Delta\lambda \approx 30$ at $\lambda = 1.2$ μm to $R > 300$ at $\lambda > 5$ μm. Object 9025 was observed with the G140M/F100LP, G235M/F170LP and G395M/F290LP medium-resolution ($R = 500$–$1,340$) gratings[51], covering 0.7–5.2 μm. Three-shutter slitlets were used, enabling a three-point nodding pattern to facilitate background subtraction. The total exposure time on sources 8595 and 9025 were the same at 3,107 s, whereas on source D36123, it was 18,387 s (approximately six times longer).

The NIRSpec data processing followed the same methodology as used for other CEERS NIRSpec observations[21,22,52–54]. The NIRSpec data reduction was based on the calibration pipeline[55] v.1.8.5 produced by the Space Telescope Science Institute and on the Calibration Reference Data System mapping 1041 for objects 8595 and 9025 and mapping 1029 for D36123. There are three main stages in the reduction process. Briefly, the calwebb_detector1 pipeline module was used to correct for the detector 1/f noise, subtract the bias and dark current, and generate the count-rate maps from the uncalibrated images. An improvement in the jump step corrects for cosmic ray 'snowballs'[22]. Stage two of the pipeline reduction creates two-dimensional spectra with a rectified trace and flat slope from the generated count-rate maps. The background subtraction and slit loss correction of objects D36123 and 8595 were applied at this stage, whereas the slit loss correction (pathloss) was not performed for object 9025 as it was poorly centred in the shutter. We verified that a better overall χ_R^2 for its spectral fit could be obtained by adopting the empirical aperture corrections directly, which is the last step of the absolute flux calibrations (as discussed later in 'Aperture correction') to complement any incorrect calibration during the reduction process. In the third stage, we used optimized apertures to extract the one-dimensional spectra in all cases. For object D36123, we adopted a 4 pixel extraction aperture to cater for the effects of bar shadows from the micro-shutter assembly[56] on some upper pixels in the two-dimensional spectra. We also considered 3 and 5 pixel apertures, with a negligible impact on the results. The flux error for the extracted spectra was calculated by the JWST pipeline using instrumental noise. We rescaled all flux errors by multiplying by a factor of ~1.5 to account for correlations induced by the pipeline[21].

The spectrum of 9025, observed with three medium-resolution gratings, was calibrated through several steps. We first matched the

three spectra, scaling them by a constant term, determined using the overlapping regions, with variance weighting. This required scaling of factors of 1.23 and 1.28 between G140M and G235M and between G235M and G395M, respectively. In the overlapping regions, the final coadded spectra were obtained by combining their weighted spectra and errors, while ensuring that standard errors in the weighted mean over common wavelength ranges remained unchanged after resampling. To increase the continuum SNR so that we could display the NIR features and speed up the spectral fit computation, we finally resampled this medium-resolution spectrum to the PRISM resolution. The average flux and the standard error of the mean in each PRISM wavelength bin were adopted.

Photometric measurements

Two out of the three galaxies (D36123 and 9025) were observed in CEERS[57] imaging with the near-infrared camera (NIRCam) onboard JWST, although all galaxies (including 8595) have CANDELS/HST imaging[23,24]. We used galfit[58,59] to derive their structure and obtain photometry in NIRCam bands (such as F115W, F150W, F200W, F277W, F356W, F410W and F444W, when available), in HST bands (such as F606W, F814W, F125W, F140W and F160W, when needed) and in the Ks band captured by the wide-field infrared camera of the Canada–France–Hawaii Telescope (only for object 8595). We adopted 3" × 3"-wide cut-outs with 0.03" pix^{-1} sampling for the NIRCam bands and 0.06" pix^{-1} sampling for the HST bands. We fitted the galaxies using single Sérsic models with free parameters, including the positions, Sérsic index (n), effective radius (r_e), total magnitudes, axis ratio (b/a) and position angle (PA). The point spread functions for different NIRCam bands were adopted from previous CEERS work[60]. They were constructed by stacking point sources using the software PSFEx[61]. We carefully modelled all objects in the field of view, paying special attention to a bright galaxy near to 8595 in the 5" × 5" region. We took into account a systematic uncertainty of about 5% in the photometry for objects D36123 and 9025, whereas a systematic uncertainty of 10% in the photometry was adopted for object 8595 when considering the effect of the bright nearby galaxy. The structural parameters (D36123 and 9025 in F150W and 8595 in F160W) are listed on Extended Data Fig. 1, which also shows the galfit models and residuals.

Aperture correction

Spectra reduced with the NIRSpec pipeline include an aperture-correction term that was derived by assuming a point-source scenario. To account for the actual shapes of our galaxies, we integrated the observed spectra through imaging filter band-passes to obtain synthetic photometry (F_{syn}), which we compared to the actual photometry (F_{phot}) measured from imaging. We implicitly assumed that no strong colour gradient biased the in-slit photometry with respect to the integrated galaxy photometry. We checked this by building colour images of our targets matched to the point spread function and verified that no colour gradients were apparent. We, thus, derived the aperture correction as $R_{corr} = F_{phot}/F_{syn}$. The top panel of Supplementary Fig. 1 shows the aperture correction for object D36123 derived in this way. We adopted a linear function to fit the trend with wavelength, as shown by the red line. There is a weak wavelength dependence (slope $\alpha \approx 0.02$). The green line is the rescaled aperture correction derived from the forward-modelling tool for NIRSpec multi-object spectroscopic data, namely MSAFIT[62], which accounted for the complex geometry of the target galaxy, point spread function and pixelation of the NIRSpec instrument. This MSAFIT line is aligned with the red line. Regardless of the relation (linear versus MSAFIT) or when adopting the extremes in the ±1σ range in the linear relation (the grey-shaded region of D36123 in Supplementary Fig. 1) used to correct the spectrum, the best-fitting parameters and spectral fits showed minimal changes. Hence, we decided to finally rescale the observed spectrum of D36123 with the linear relation. The same process was applied to the other two objects, 8595 and 9025. Their spectra were

rescaled by multiplying by a constant value of -2.28 and by using a linear relation with a slope of approximately −0.07, respectively.

Spectral resolution

When comparing the observed spectra with spectral synthesis models, we need to match their spectral resolutions. For the observed spectra, we accounted for the instrumental broadening and for the intrinsic linewidths from the galaxies. For the template models, we estimated their intrinsic spectral resolution. We will discuss these terms in the following.

The spectral resolution of NIRSpec PRISM was relatively low. Based on spectral sampling and for an unresolved source filling the slit, we expected a resolution of 70 at 0.6 μm, declining to 30 at 1.1 μm and rising again to 200 at 5 μm. For point and compact sources, the resolution of in-flight data could be ×1.5–2.0 higher than that in the prelaunch approximation[62]. This would be helpful for identifying weak or narrower features, especially for galaxy D36123, as the SNR in the continuum was high. We used the MSAFIT[62] software to model the NIRSpec resolving power based on the galaxy's actual spatial profile. The resolution modelled by MSAFIT software is consistent with that of a flat source in a slit width of 1.4 pixels (green curve in the top middle panel of Supplementary Fig. 2).

We next accounted for the intrinsic dispersion of our target ETGs. The velocity dispersion σ was estimated using local stellar mass versus velocity dispersion relations (M_* versus σ)[33]. We converted σ to the full-width at half-maximum and defined $1/R = v_{(rest, FWHM)}/c = \Delta\lambda/\lambda$, where $\Delta\lambda$ equals the full-width at half-maximum. The intrinsic broadening of an ETG with a velocity dispersion of ~130 km s^{-1} (a ballpark number for the typical masses ~$10^{10} M_\odot$ in our study) corresponded to $R \approx 1,000$ (grey line in the top middle panel of Supplementary Fig. 2), which was quite negligible compared to the instrumental spread.

Finally, we estimated the template model's resolution from the spectral sampling, adopting two spectral bin widths as their (Nyquist) sampling. The sampling (hence, resolution) was changed in steps that were higher in the optical than in the NIR. Redshifting affected where these steps actually applied for the observed galaxies. The corresponding resolution in the observed frame for D36123 (using $z = 1.08$) is shown in the top middle panel of Supplementary Fig. 2.

To match the resolution of the models with the observed spectrum, we accounted for all three factors: PRISM dispersion (dominant term), the wavelength sampling of the spectral template models and the velocity dispersion of the ETG. We added and subtracted in quadrature the corresponding terms at fixed λ_{obs}. Broadening $\Delta\lambda_{fit}$ was applied to the models to match the observed spectra:

$$\Delta\lambda_{fit} = \sqrt{\Delta\lambda^2_{PRISM(1.4\,pix)} - \Delta\lambda^2_{MOD_i} + \Delta\lambda^2_{ETG}}, \qquad (1)$$

where i refers to the model. The final smoothing functions applied to the models were equivalent to resolutions ranging from $R \approx 50$ to 400 across the observed wavelength range of 0.6–3.3 μm, as depicted in the top right panel of Supplementary Fig. 2. Beyond ~3 μm for some models, we were limited by the models' resolution. No further smoothing was applied to those. We repeated a similar procedures to obtain the appropriate smoothing kernels for objects 8595 and 9025, as shown in the middle and bottom panels of Supplementary Fig. 2. For both, the PRISM resolution was based on 1.4 pixel elements, and the spectra in different models were resampled in every two spectral bin widths, as was done for object D36123.

Spectral fit

To estimate the stellar mass, age and SFH of a galaxy, we adopted a custom IDL routine[63] to fit the final corrected one-dimensional spectrum of each galaxy. The best-fitting results were derived by comparing the one-dimensional spectrum with a range of composite stellar population templates by minimizing χ^2. These templates were generated by combining a grid of different SSP models and assuming a delayed

exponentially declining SFH ($\propto (t/\tau^2)e^{-t/\tau}$, the delayed-$\tau$ model). The characteristic timescale τ and age variations (the time t since the onset of star formation) were the same in different models, as shown in Supplementary Table 2. To identify the redshift, the Calzetti attenuation law[64] was adopted. The stellar metallicity was left free with lower and upper limits dependent on the model. To reduce the computational cost, we ran the spectral fit twice. First, we ran the spectral fit over a large range of redshifts with a low-resolution grid ($\Delta z = 0.1$). Once the most probable redshift peak had been identified, we narrowed down the redshift range and used a high-resolution grid ($\Delta z = 0.001$) in the second run. The redshift boundary in Supplementary Table 2 is an example of a parametric grid for D36123 in the second run. For object D36123, which had the highest SNR, the spectral fit was repeated by varying the wavelength range (Table 1): (1) with the full rest-frame wavelength (0.3–2.0 μm; Extended Data Fig. 2a–d), (2) with the optical only ($\lambda_{\mathrm{rest}} < 0.5$ μm), (3) with the NIR only ($\lambda_{\mathrm{rest}} > 0.5$ μm) and (4) with the full rest-frame wavelength range but excluding 0.5–1.0 μm (Extended Data Fig. 2e–h). For the two fainter galaxies, the spectral fit was done only for the full rest-frame wavelength. As the medium-resolution grating spectrum used for object 9025 did not cover too well the age-sensitive spectral region around the rest-frame 4,000 Å break, we additionally used the photometry in the HST F606W and F814W bands to better constrain the overall fit.

The best-fitting parameters with 1σ errors[65] were derived from the distribution of χ^2, as listed in Table 2. Considering the large minimum reduced χ^2 of object D36123, we derived the uncertainties (Table 1), scaling up all errors to obtain $\chi^2_R \approx 1.0$. Stellar masses are reported for a Chabrier initial mass function (IMF)[66]. These were corrected for stellar losses and include remnants. Ages reported in the tables and discussed in the paper are mass-weighted. Extended Data Fig. 2 shows the best-fitting model for each galaxy in red at the top of each panel and the relative flux deviation $D_{\mathrm{REL}} = (F_{\lambda,\mathrm{obs}} - F_{\lambda,\mathrm{mod}})/F_{\lambda,\mathrm{obs}}$ at the bottom of each panel. The SNR-weighted averages of the relative deviations are labelled at the top of each bottom panel. For object D36123, the models deviated from the spectrum at a few percent levels (by 2.5% for M13 and higher values for the other models). This was probably driven by systematics in the models (plus, possible residual calibration errors), which we could detect at the high SNR. Higher deviations correspond to observed features not matched by the models. For the other galaxies, the relative flux deviations were larger and dominated by the noise in the data.

Fitting other models to D36123. In addition to the models discussed in the main text, we also fitted three other models to the galaxy D36123, including two fully empirical sets of models, XSL[35] and E-MILES[36]. We also tested CB07 models (https://www.bruzual.org/cb07/), an update of BC03 that was meant to include strong TP-AGB (never formally published). A description of the recipes of these models is provided in 'Further details of model input' in Methods. Their intrinsic dispersion and resolutions are shown in the top panels of Supplementary Fig. 2. Both the XSL and E-MILES models have higher intrinsic resolutions than the other models. The parameter grid settings in these three models are the same as those of the four main models, except for the metallicity due to available ranges (see Supplementary Table 2 for details). Their corresponding best-fitting models are displayed in Extended Data Fig. 3, and the best-fitting redshift, mass-weighted age, stellar mass and reduced χ^2_R are shown in Extended Data Table 2, but only for the full-range fits. The XSL model does not cover the blueward of $\lambda_{\mathrm{rest}} = 3,500$ Å and includes two noisy regions corresponding to the low atmospheric transmission, which were masked during the spectral fit (grey-shaded regions of Extended Data Fig. 3).

Selected features and indices for D36123

We provide quantitative measurements of a range of features and indices for D36123, which were chosen to be particularly representative as a test of the underlying contributing stellar phases and also of

the models. These take into account the fairly reduced resolution of the PRISM spectrum of D36123, which triggered an ad hoc redefinition of some indices, even when similar indices were already defined in the literature. However, by measuring these indices in the same way in the matched-resolution best-fitting models as well in representative stellar phases also at matched resolutions (including C- and O-rich TP-AGB[13,14] and RGB[35]), we gained some valuable scientific insights (Fig. 3).

We defined two EW indices, estimated with the equation:

$$EW(\lambda) = \int_{\lambda_1}^{\lambda_2} \frac{F_c - F_\lambda}{F_c}\, d\lambda, \qquad (2)$$

where F_c is the continuum obtained by drawing a straight line (blue dashed lines in Fig. 3a,b) between the two-side average continuum from λ_1 to λ_2, estimated over 100 Å (rest) regions (red crosses).

(1) EW (0.50–0.53 μm) index: This includes the Mg I and Mg II features. It overlaps the Mg II index but also includes TiO and CN features. The continuum side windows are for the rest-frame ranges 0.50–0.51 μm and 0.53–0.54 μm, whereas the index was integrated over rest-frame range 0.51–0.53 μm.

(2) EW (0.9–1.0 μm) index: This covers the TiO + ZrO 'valley' and the CN0.92 edge. The continuum side windows are for the rest-frame ranges 0.91–0.92 μm and 0.98–0.99 μm, whereas the index was integrated over rest-frame range 0.920–0.986 μm.

We further defined two strength indices as follows:

(3) The H-bump index. This broad bump, sensitive to the presence of cool stars, is the combination of the H$^-$ peak opacity at 1.6 μm and of H$_2$O vapour absorptions around 1.4 and 1.9 μm. We adopted the literature definition[67]:

$$I(\text{H bump}) = -2.5 \log\left[\left(\frac{1}{\lambda_2 - \lambda_1}\right) \int_{\lambda_1}^{\lambda_2} \frac{F_\lambda}{F_{\mathrm{cont}}}\, d\lambda\right]. \qquad (3)$$

The pseudo-continuum flux F_{cont} (blue dashed line in Fig. 3c) was estimated by connecting the midpoint of the two-side continuum windows for rest-frame ranges 1.45–1.47 μm and 1.765–1.785 μm (red crosses). F_λ was integrated from $\lambda_1 = 1.61$ μm to $\lambda_2 = 1.67$ μm.

(4) The CN1.1 index. Among all CN edges, CN1.1 was the strongest detection in D36123. We defined the CN1.1 index as follows:

$$I(\text{CN1.1}) = -2.5 \log\langle F'_{\mathrm{cont}}/F_\lambda\rangle, \qquad (4)$$

where the pseudo-continuum F'_{cont} has a normalization and slope that were both measured using a single window at rest wavelengths bluer than the edge between ~1.05 and 1.075 μm and was ~250 Å wide. We needed to define a slope to allow us to distinguish a steeply declining continuum over a large range from genuine edge-like discontinuities. A positive (rising slope) was, however, reset to a flat continuum to avoid artificially inflating the index. We then extrapolated this pseudo-continuum for the range ~1.10–1.12 μm over which we integrated the spectrum (Fig. 3d).

Index measurements for D36123, best-fitting models and stellar templates of interest are shown in Fig. 3. All the measurements are also listed in Extended Data Table 1. Measurements from models have, obviously, no associated uncertainties.

Further details of model input

The BC03 models[8] were calculated with an isochrone synthesis algorithm, using Padova and Geneva tracks plus extra ingredients to describe the TP-AGB phase. They adopted both theoretical (BaSeL) and observational (STELIB and Pickles) libraries of stellar spectra. The STELIB and Pickles libraries were extended to shorter and longer wavelengths using BaSeL. The CB07 (and CB16) models (https://www.bruzual.org/) are updated versions of the BC03 model. The C09 models

have several user options, and they have been modified through the years. The models used in this work were generated using the latest version of FSPS v.3.2 by adopting a Chabrier IMF, the BaSTI isochrones and the MILES stellar library in the optical. The C09 models include TP-AGB spectra, extrapolated blueward with simpler linear slopes (as advocated by Lançon & Wood[13]) and redward with the Aringer et al.[68,69] synthetic carbon star spectral library. The spectra of the oxygen-rich TP-AGB stars were extrapolated with the latest version of the PHOENIX stellar spectral library (BT-SETTL library). For the TP-AGB isochrones, no shift was adopted for $\log(L_{bol})$ versus $\log(T_{eff})$. The Maraston models (M05 and M13) use the fuel-consumption theorem for the post-main-sequence phases[3] and adopt empirical C- and O-rich spectra for the TP-AGB phase[13,14] and the BaSeL library for the other phases. The XSL model[35] used the PARSEC/COLIBRI isochrones, including a TP-AGB contribution, and adopted the XSL, which contained many evolved cool giants and covered the wavelength range from 3,500 Å to 2.48 μm (shorter than other models). These cool giants with $T_{eff} < 4,000$ K were incorporated into the XSL model by using the average spectra of static giants (RGB) and O- and C-rich TP-AGB stars, binned by broadband colour in the Vega system. The E-MILES model[36] adopted BaSTI stellar tracks for all phases, including the TP-AGB. The E-MILES library (http://miles.iac.es/pages/) was used for stellar spectra. In this work, all models assumed a Chabrier IMF and were corrected to a solar metallicity $Z_\odot = 0.02$. To gain a crude understanding of the effect of TP-AGB stars in the NIR mass-to-light ratio, we show in Supplementary Fig. 3, the ~1 Gyr SSP models around solar metallicity from the different libraries. SSPs from the CB16, Vazdekis, XSL, E-MILES and CB07 models were degraded to match the wavelength-dependent resolution of M13 for better visualization.

Data availability

The JWST NIRSpec data are available from the Mikulski Archive for Space Telescope (http://archive.stsci.edu), under programme IDs 1345 and 2750. The CEERS JWST imaging data are available from the Mikulski Archive for Space Telescope under programme ID 1345. Reduced NIRCam data products from the CEERS team are available at https://ceers.github.io. The HST imaging data are available from the CANDELS survey at https://archive.stsci.edu/hlsp/candels, and the NIRCam/Ks imaging data are published in the 3D-HST survey at https://archive.stsci.edu/prepds/3d-hst/.

Code availability

The JWST NIRSpec data were reduced using the JWST pipeline (v.1.8.5, reference mappings 1041 and 1029; https://github.com.spacetelescope/jwst). The MSAFIT software is available at https://github.com/annadeg/jwst-msafit. The galfit software is published at https://users.obs.carnegiescience.edu/peng/work/galfit/galfit.html.

References

1. Renzini, A. Energetics of stellar populations. *Ann. Phys.* **6**, 87–102 (1981).
2. Renzini, A. & Voli, M. Advanced evolutionary stages of intermediate mass stars. I. Evolution of surface compositions. *Astron. Astrophys.* **94**, 175 (1981).
3. Maraston, C. Evolutionary synthesis of stellar populations: a modular tool. *Mon. Not. R. Astron. Soc.* **300**, 872–892 (1998).
4. Maraston, C. Evolutionary population synthesis: models, analysis of the ingredients and application to high-z galaxies. *Mon. Not. R. Astron. Soc.* **362**, 799–825 (2005).
5. Salaris, M., Weiss, A., Cassarà, L. P., Piovan, L. & Chiosi, C. Detailed AGB evolutionary models and near-infrared colours of intermediate-age stellar populations: tests on star clusters. *Astron. Astrophys.* **565**, A9 (2014).
6. Maraston, C. et al. Evidence for TP-AGB stars in high-redshift galaxies, and their effect on deriving stellar population parameters. *Astrophys. J.* **652**, 85–96 (2006).
7. Tonini, C., Maraston, C., Devriendt, J., Thomas, D. & Silk, J. The impact of thermally pulsing asymptotic giant branch stars on hierarchical galaxy formation models. *Mon. Not. R. Astron. Soc.* **396**, L36–L40 (2009).
8. Bruzual, G. & Charlot, S. Stellar population synthesis at the resolution of 2003. *Mon. Not. R. Astron. Soc.* **344**, 1000–1028 (2003).
9. Marigo, P. et al. Evolution of asymptotic giant branch stars. II. Optical to far-infrared isochrones with improved TP-AGB models. *Astron. Astrophys.* **482**, 883–905 (2008).
10. Conroy, C., Gunn, J. E. & White, M. The propagation of uncertainties in stellar population synthesis modeling. I. The relevance of uncertain aspects of stellar evolution and the initial mass function to the derived physical properties of galaxies. *Astrophys. J.* **699**, 486–506 (2009).
11. Noël, N. E. D., Greggio, L., Renzini, A., Carollo, C. M. & Maraston, C. Calibrating stellar population models with Magellanic Cloud star clusters. *Astrophys. J.* **772**, 58 (2013).
12. Pastorelli, G. et al. Constraining the thermally pulsing asymptotic giant branch phase with resolved stellar populations in the Large Magellanic Cloud. *Mon. Not. R. Astron. Soc.* **498**, 3283–3301 (2020).
13. Lançon, A. & Wood, P. R. A library of 0.5 to 2.5 μm spectra of luminous cool stars. *Astron. Astrophys. Suppl. Ser.* **146**, 217–249 (2000).
14. Lançon, A. & Mouhcine, M. The modelling of intermediate-age stellar populations. II. Average spectra for upper AGB stars, and their use. *Astron. Astrophys.* **393**, 167–181 (2002).
15. Girardi, L., Bressan, A., Bertelli, G. & Chiosi, C. Evolutionary tracks and isochrones for low- and intermediate-mass stars: From 0.15 to 7 M_{sun}, and from Z = 0.0004 to 0.03. *Astron. Astrophys. Suppl. Ser.* **141**, 371–383 (2000).
16. Kriek, M. et al. The spectral energy distribution of post-starburst galaxies in the NEWFIRM medium-band survey: a low contribution from TP-AGB stars. *Astrophys. J. Lett.* **722**, L64–L69 (2010).
17. Zibetti, S., Gallazzi, A., Charlot, S., Pierini, D. & Pasquali, A. Near-infrared spectroscopy of post-starburst galaxies: a limited impact of TP-AGB stars on galaxy spectral energy distributions. *Mon. Not. R. Astron. Soc.* **428**, 1479–1497 (2013).
18. Riffel, R. et al. The stellar spectral features of nearby galaxies in the near infrared: tracers of thermally pulsing asymptotic giant branch stars? *Mon. Not. R. Astron. Soc.* **450**, 3069–3079 (2015).
19. Capozzi, D. et al. Revisiting the role of the thermally pulsating asymptotic-giant-branch phase in high-redshift galaxies. *Mon. Not. R. Astron. Soc.* **456**, 790–830 (2016).
20. Finkelstein, S. L. et al. CEERS key paper. I. An early look into the first 500 Myr of galaxy formation with JWST. *Astrophys. J. Lett.* **946**, L13 (2023).
21. Arrabal Haro, P. et al. Spectroscopic confirmation of CEERS NIRCam-selected galaxies at z=8–10. *Astrophys. J. Lett.* **951**, L22 (2023).
22. Arrabal Haro, P. et al. Confirmation and refutation of very luminous galaxies in the early Universe. *Nature* **622**, 707–711 (2023).
23. Grogin, N. A. et al. CANDELS: The Cosmic Assembly Near-infrared Deep Extragalactic Legacy Survey. *Astrophys. J. Suppl. Ser.* **197**, 35 (2011).
24. Koekemoer, A. M. et al. CANDELS: The Cosmic Assembly Near-infrared Deep Extragalactic Legacy Survey—The Hubble Space Telescope observations, imaging data products, and mosaics. *Astrophys. J. Suppl. Ser.* **197**, 36 (2011).
25. Stefanon, M. et al. CANDELS multi-wavelength catalogs: source identification and photometry in the CANDELS extended Groth strip. *Astrophys. J. Suppl. Ser.* **229**, 32 (2017).
26. Whitaker, K. E. et al. The NEWFIRM medium-band survey: photometric catalogs, redshifts, and the bimodal color distribution of galaxies out to z~3. *Astrophys. J.* **735**, 86 (2011).

27. Onodera, M. et al. The ages, metallicities, and element abundance ratios of massive quenched galaxies at z≈1.6. *Astrophys. J.* **808**, 161 (2015).

28. Lançon, A., Goldader, J. D., Leitherer, C. & González Delgado, R. M. Multiwavelength study of the starburst galaxy NGC 7714. II. The balance between young, intermediate-age, and old stars. *Astrophys. J.* **552**, 150–167 (2001).

29. Habing, H. J. & Olofsson, H. *Asymptotic Giant Branch Stars* (Springer New York, 2004).

30. Riffel, R., Pastoriza, M. G., Rodríguez-Ardila, A. & Maraston, C. The first detection of near-infrared CN bands in active galactic nuclei: signature of star formation. *Astrophys. J. Lett.* **659**, L103–L106 (2007).

31. Rayner, J. T., Cushing, M. C. & Vacca, W. D. The infrared telescope facility (IRTF) spectral library: cool stars. *Astrophys. J. Suppl. Ser.* **185**, 289–432 (2009).

32. Faber, S. M., Friel, E. D., Burstein, D. & Gaskell, C. M. Old stellar populations. II. An analysis of K-giant spectra. *Astrophys. J. Suppl. Ser.* **57**, 711–741 (1985).

33. Thomas, D., Maraston, C., Bender, R. & Mendes de Oliveira, C. The epochs of early-type galaxy formation as a function of environment. *Astrophys. J.* **621**, 673–694 (2005).

34. Ferraro, F. R., Origlia, L., Testa, V. & Maraston, C. Probing the red giant branch phase transition: near-infrared photometry of six intermediate-age Large Magellanic Cloud clusters. *Astrophys. J.* **608**, 772–780 (2004).

35. Verro, K. et al. Modelling simple stellar populations in the near-ultraviolet to near-infrared with the X-shooter Spectral Library (XSL). *Astron. Astrophys.* **661**, A50 (2022).

36. Vazdekis, A. et al. Evolutionary stellar population synthesis with MILES. II. Scaled-solar and α-enhanced models. *Mon. Not. R. Astron. Soc.* **449**, 1177–1214 (2015).

37. Baldwin, C., McDermid, R. M., Kuntschner, H., Maraston, C. & Conroy, C. Comparison of stellar population model predictions using optical and infrared spectroscopy. *Mon. Not. R. Astron. Soc.* **473**, 4698–4721 (2018).

38. Dahmer-Hahn, L. G. et al. Probing evolutionary population synthesis models in the near infrared with early-type galaxies. *Mon. Not. R. Astron. Soc.* **476**, 4459–4480 (2018).

39. Eftekhari, E., La Barbera, F., Vazdekis, A., Allende Prieto, C. & Knowles, A. T. Strong CO absorption features in massive ETGs. *Mon. Not. R. Astron. Soc.* **512**, 378–400 (2022).

40. Riffel, R. et al. Erratum: optical/NIR stellar absorption and emission-line indices from luminous infrared galaxies. *Mon. Not. R. Astron. Soc.* **486**, 5074–5074 (2019).

41. Conroy, C. & Gunn, J. E. The propagation of uncertainties in stellar population synthesis modeling. III. Model calibration, comparison, and evaluation. *Astrophys. J.* **712**, 833–857 (2010).

42. Lonoce, I. et al. Old age and supersolar metallicity in a massive z~1.4 early-type galaxy from VLT/X-Shooter spectroscopy. *Mon. Not. R. Astron. Soc.* **454**, 3912–3919 (2015).

43. Johansson, J., Thomas, D. & Maraston, C. Chemical element ratios of Sloan Digital Sky Survey early-type galaxies. *Mon. Not. R. Astron. Soc.* **421**, 1908–1926 (2012).

44. Worthey, G., Tang, B. & Serven, J. Individual alpha elements, C, N, and Ba in early-type galaxies. *Astrophys. J.* **783**, 20 (2014).

45. Conroy, C., Graves, G. J. & van Dokkum, P. G. Early-type galaxy archeology: ages, abundance ratios, and effective temperatures from full-spectrum fitting. *Astrophys. J.* **780**, 33 (2014).

46. Parikh, T. et al. SDSS-IV MaNGA: the spatially resolved stellar initial mass function in ~400 early-type galaxies. *Mon. Not. R. Astron. Soc.* **477**, 3954–3982 (2018).

47. Worthey, G., Faber, S. M. & Gonzalez, J. J. Mg and Fe absorption features in elliptical galaxies. *Astrophys. J.* **398**, 69 (1992).

48. Thomas, D., Maraston, C. & Bender, R. Stellar population models of Lick indices with variable element abundance ratios. *Mon. Not. R. Astron. Soc.* **339**, 897–911 (2003).

49. Schneider, R. & Maiolino, R. The formation and cosmic evolution of dust in the early Universe. I. Dust sources. *Astron. Astrophys. Rev.* **32**, 2 (2024).

50. Kelson, D. D. & Holden, B. P. The mid-infrared luminosities of normal galaxies over cosmic time. *Astrophys. J. Lett.* **713**, L28–L32 (2010).

51. Jakobsen, P. et al. The near-infrared spectrograph (NIRSpec) on the James Webb Space Telescope. I. Overview of the instrument and its capabilities. *Astron. Astrophys.* **661**, A80 (2022).

52. Fujimoto, S. et al. CEERS spectroscopic confirmation of NIRCam-selected z≳8 galaxy candidates with JWST/NIRSpec: initial characterization of their properties. *Astrophys. J. Lett.* **949**, L25 (2023).

53. Kocevski, D. D. et al. Hidden little monsters: spectroscopic identification of low-mass, broad-line AGNs at z>5 with CEERS. *Astrophys. J. Lett.* **954**, L4 (2023).

54. Larson, R. L. et al. A CEERS discovery of an accreting supermassive black hole 570 Myr after the Big Bang: identifying a progenitor of massive z>6 quasars. *Astrophys. J. Lett.* **953**, L29 (2023).

55. Bushouse, H. et al. *JWST Calibration Pipeline* (STScI, 2022).

56. Ferruit, P. et al. The near-infrared spectrograph (NIRSpec) on the James Webb Space Telescope. II. Multi-object spectroscopy (MOS). *Astron. Astrophys.* **661**, A81 (2022).

57. Finkelstein, S. L. et al. A long time ago in a galaxy far, far away: a candidate z~12 galaxy in early JWST CEERS imaging. *Astrophys. J. Lett.* **940**, L55 (2022).

58. Peng, C. Y., Ho, L. C., Impey, C. D. & Rix, H.-W. Detailed structural decomposition of galaxy images. *Astron. J.* **124**, 266–293 (2002).

59. Peng, C. Y., Ho, L. C., Impey, C. D. & Rix, H.-W. Detailed decomposition of galaxy images. II. Beyond axisymmetric models. *Astron. J.* **139**, 2097–2129 (2010).

60. Gómez-Guijarro, C. et al. JWST CEERS probes the role of stellar mass and morphology in obscuring galaxies. *Astron. Astrophys.* **677**, A34 (2023).

61. Bertin, E. in *Astronomical Data Analysis Software and Systems XX* Vol. 442 (eds Evans, I. N. et al.) 435 (ASP, 2011).

62. de Graaff, A. et al. Ionised gas kinematics and dynamical masses of z≳6 galaxies from JADES/NIRSpec high-resolution spectroscopy. *Astron. Astrophys.* **684**, A87 (2024).

63. Gobat, R. et al. The early early type: discovery of a passive galaxy at z_spec ~3. *Astrophys. J. Lett.* **759**, L44 (2012).

64. Calzetti, D. et al. The dust content and opacity of actively star-forming galaxies. *Astrophys. J.* **533**, 682–695 (2000).

65. Avni, Y. Energy spectra of X-ray clusters of galaxies. *Astrophys. J.* **210**, 642–646 (1976).

66. Chabrier, G. Galactic stellar and substellar initial mass function. *Publ. Astron. Soc. Pac.* **115**, 763–795 (2003).

67. Worthey, G., Faber, S. M., Gonzalez, J. J. & Burstein, D. Old stellar populations. V. Absorption feature indices for the complete Lick/IDS sample of stars. *Astrophys. J. Suppl. Ser.* **94**, 687 (1994).

68. Aringer, B., Girardi, L., Nowotny, W., Marigo, P. & Lederer, M. T. Synthetic photometry for carbon rich giants. I. Hydrostatic dust-free models. *Astron. Astrophys.* **503**, 913–928 (2009).

69. Riffel, R., Pastoriza, M. G., Rodríguez-Ardila, A. & Bonatto, C. Probing the near-infrared stellar population of Seyfert galaxies. *Mon. Not. R. Astron. Soc.* **400**, 273–290 (2009).

Acknowledgements

Author contributions

S.L. and E.D. conceived this project, and selected and identified galaxies. S.L. led the analysis, and together with E.D., C.M. and M.D., wrote the manuscript. P.A.H. and M.D. led the original observations and reduced the NIRSpec spectra. R.G. wrote the fitting code and with C.D.E. helped with the spectral fitting procedures. All authors aided in the analysis and interpretation and contributed to the final manuscript.

Competing interests

The authors declare no competing interests.

Additional information

Extended data is available for this paper at https://doi.org/10.1038/s41550-024-02391-9.

Supplementary information The online version contains supplementary material available at https://doi.org/10.1038/s41550-024-02391-9.

Correspondence and requests for materials should be addressed to Shiying Lu, Emanuele Daddi or Claudia Maraston.

Peer review information *Nature Astronomy* thanks Rogério Riffel, Ambra Nanni and the other, anonymous, reviewer(s) for their contribution to the peer review of this work.
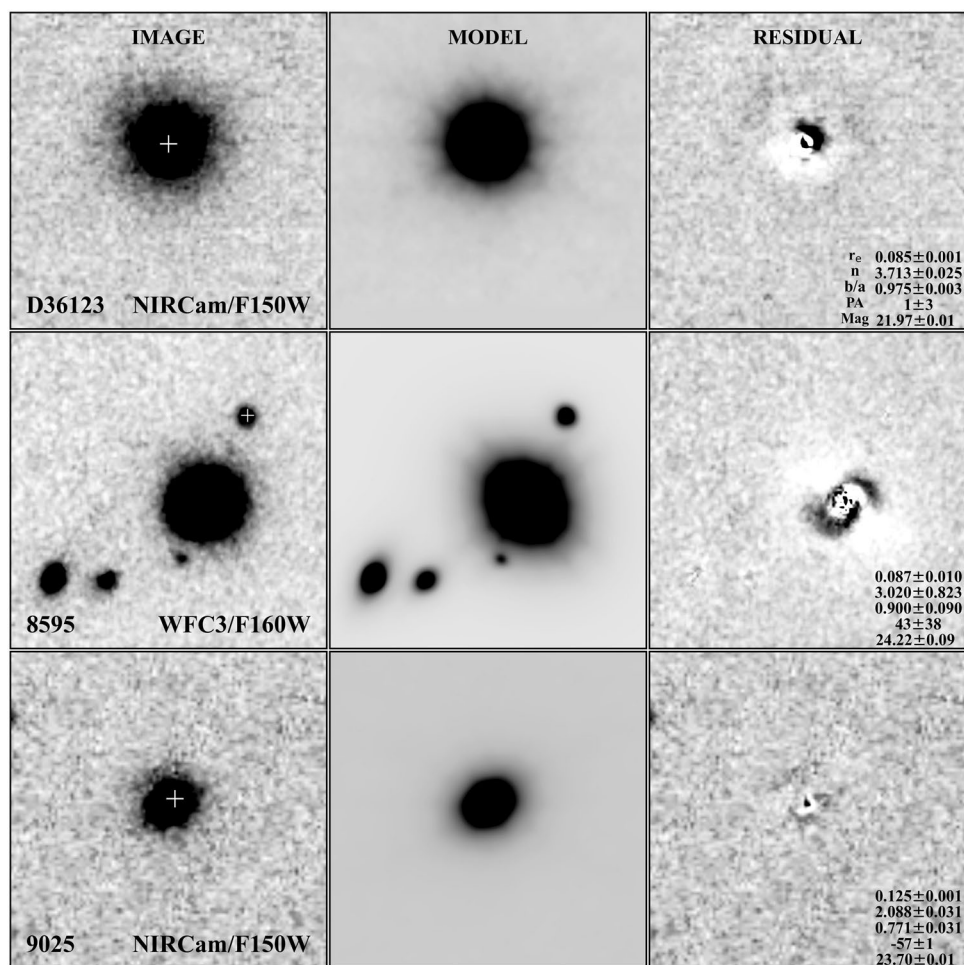
Reprints and permissions information is available at www.nature.com/reprints.

¹School of Astronomy and Space Science, Nanjing University, Nanjing, China. ²Université Paris-Saclay, Université Paris Cité, CEA, CNRS, AIM, Paris, France. ³Key Laboratory of Modern Astronomy and Astrophysics (Nanjing University), Ministry of Education, Nanjing, China. ⁴Institute of Cosmology and Gravitation, University of Portsmouth, Portsmouth, UK. ⁵NSF's National Optical-Infrared Astronomy Research Laboratory, Tucson, AZ, USA. ⁶Instituto de Física, Pontificia Universidad Católica de Valparaíso, Valparaíso, Chile. ⁷INAF-Osservatorio Astronomico di Padova, Padua, Italy. ⁸University of Massachusetts Amherst, Amherst, MA, USA. ⁹Department of Astronomy, The University of Texas at Austin, Austin, TX, USA. ¹⁰INAF-Osservatorio Astronomico di Roma, Monte Porzio Catone, Italy. ¹¹Department of Physics and Astronomy, University of California, Riverside, CA, USA. ¹²Instituto de Astrofísica de Canarias (IAC), La Laguna, Spain. ¹³Universidad de la Laguna, La Laguna, Spain. ¹⁴Space Telescope Science Institute, Baltimore, MD, USA. ¹⁵Université Paris-Cité, LERMA - Observatoire de Paris, PSL, Paris, France. ¹⁶Laboratory for Multiwavelength Astrophysics, School of Physics and Astronomy, Rochester Institute of Technology, Rochester, NY, USA. ¹⁷Department of Physics, University of California, Merced, Merced, CA, USA. ¹⁸Department of Physics and Astronomy, Texas A&M University, College Station, TX, USA. ¹⁹George P. and Cynthia Woods Mitchell Institute for Fundamental Physics and Astronomy, Texas A&M University, College Station, TX, USA. ²⁰ESA/AURA Space Telescope Science Institute, Baltimore, MD, USA. ²¹Department of Physics and Astronomy, University of California, Los Angeles, CA, USA. ²²Kavli Institute for Cosmology, University of Cambridge, Cambridge, UK. ²³Cavendish Laboratory, University of Cambridge, Cambridge, UK. ✉e-mail: ShiyingLu@smail.nju.edu.cn; emanuele.daddi@cea.fr; claudia.maraston@port.ac.uk

IMAGE	MODEL	RESIDUAL

D36123   NIRCam/F150W

r_e 0.085±0.001
n 3.713±0.025
b/a 0.975±0.003
PA   1±3
Mag   21.97±0.01

8595   WFC3/F160W

0.087±0.010
3.020±0.823
0.900±0.090
43±38
24.22±0.09

9025   NIRCam/F150W

0.125±0.001
2.088±0.031
0.771±0.031
-57±1
23.70±0.01

Extended Data Fig. 1 | Example of galfit results. The original image, best-fit model, and residual of object D36123 in NIRCam/F150W are shown in the top row. The results of objects 8595 in WFC3/F160W and 9025 in NIRCam/F150W are presented in the middle and bottom rows, respectively. The three targets are marked by white crosses on the original images (notice that 8595 is not at the center of the cutout). The cutouts of objects D36123 and 9025 are 3″ × 3″ wide, with a scale of 0.03″/pix. The cutouts for object 8595 are 5″ × 5″ wide with a pixel scale of 0.06″/pix. The best-fit structural parameters of each object are shown at the bottom of each residual panel, including the effective radius (r_e) in arcsec, Sérsic index (n), axis ratio (b/a), position angle (PA) in degree, and AB Magnitude.
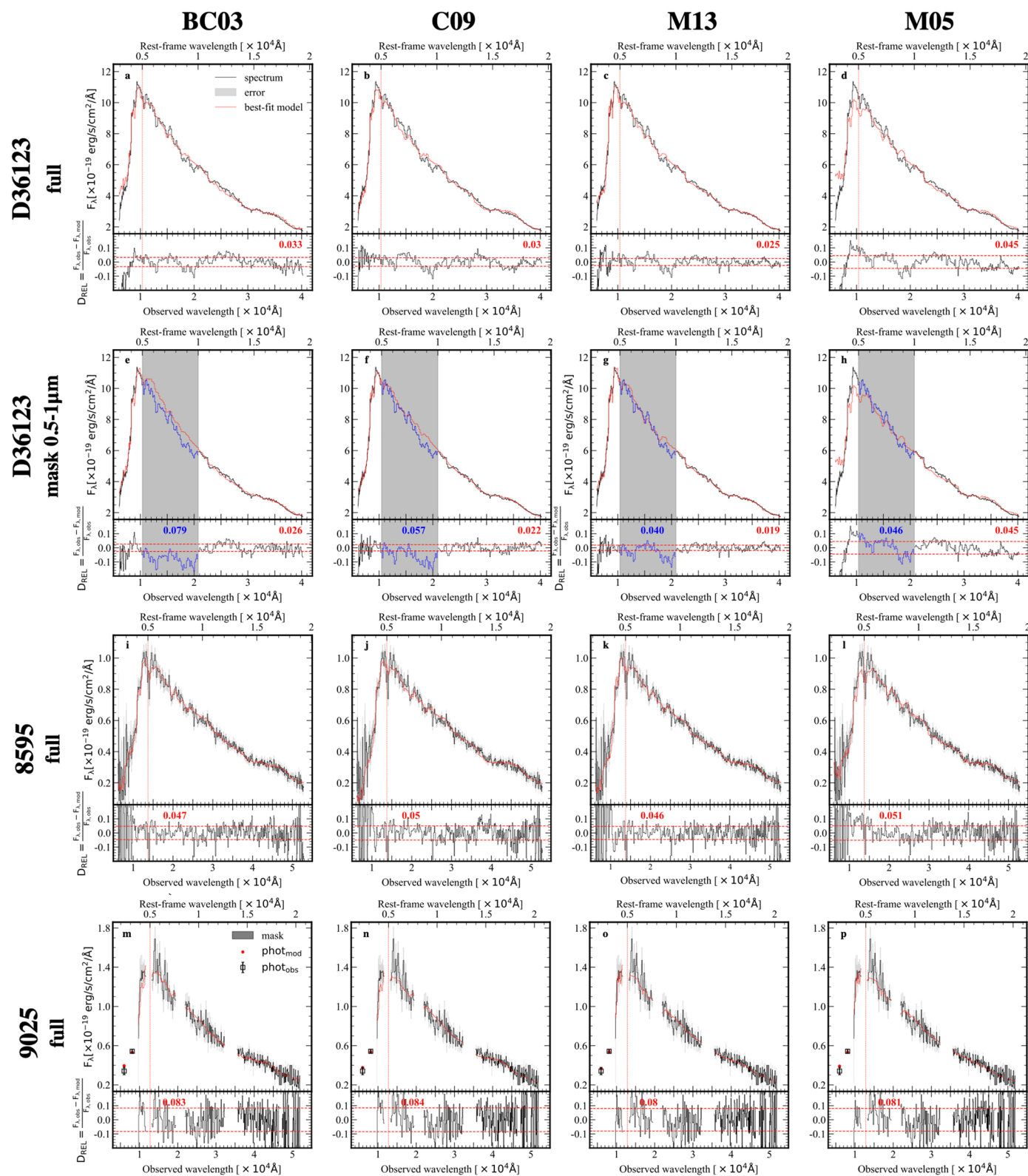
Extended Data Fig. 2 | Best-fit results and relative deviations. From left to right, the best fits (top) and relative deviations (bottom) obtained by fitting BC03, C09, M13, and M05 models are shown. The panels from top to bottom present the results corresponding to D36123 in the full fit (1st) and in masking 0.5-1μm fit (2nd), 8595 (3rd) and 9025 (4th) in the full fit, respectively. The red horizontal dashed lines are the SNR-weighted mean of the relative deviation in the fitted region, and the corresponding value within the fitted (masked) region is printed in red (blue) on the top of each bottom panel. Detector defects in the spectrum of object 9025 are masked by grey rectangles.
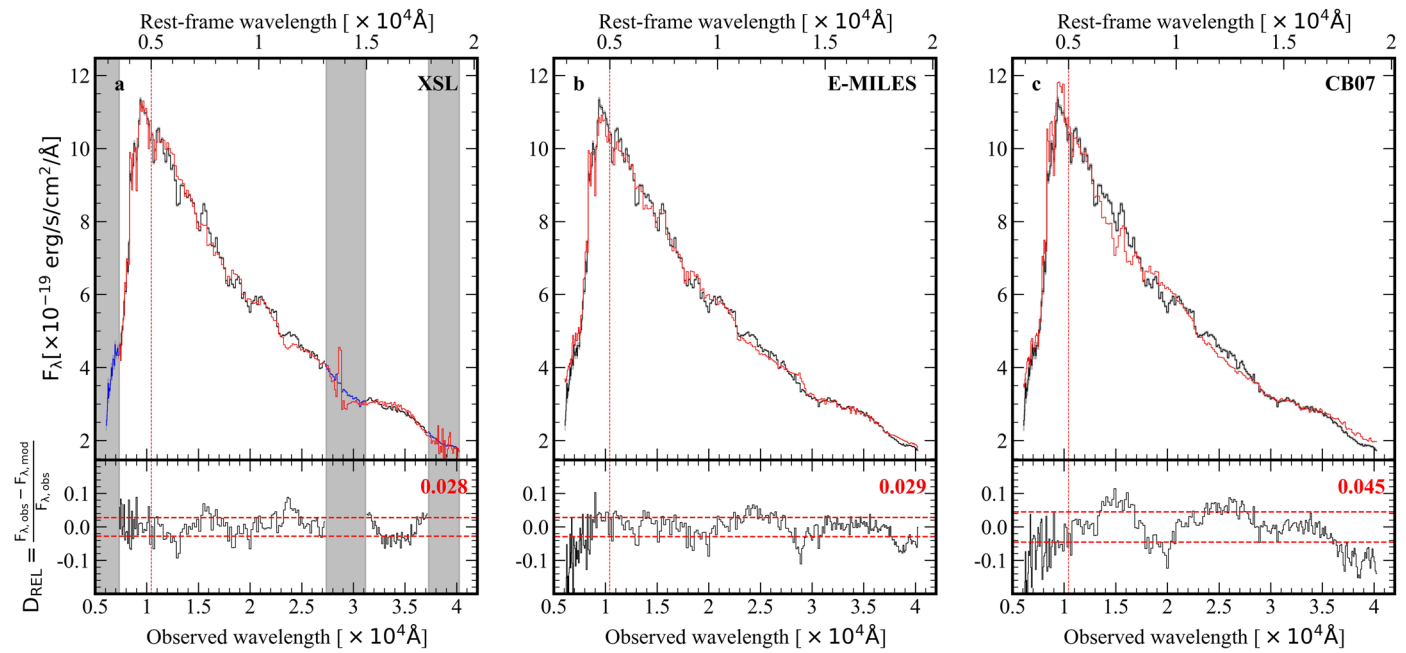
Extended Data Fig. 3 | Best-fitting spectra and relative deviations for D36123 based on XSL, E-MILES, and CB07 models. Analogous to Extended Data Fig. 2. The grey-shaded areas in the XSL model show the uncovered region at a short wavelength and two noisy telluric regions at a longer wavelength.

Extended Data Table 1 | Selected indexes and features quantitatively measured

Spec	Bin	H-bump index 1.61-1.67μm	CN1.1 index ~1.1μm	EW(Mg+TiO+C$_2$) 0.5-0.53μm	EW(CN0.92+TiO+ZrO) 0.9-1μm
D36123	–	-0.084±0.002	-0.116±0.003	9.639±0.486	33.569±0.944
BC03	–	-0.048	-0.014	5.246	6.934
C09	–	-0.143	-0.036	4.933	12.716
M13	–	-0.115	-0.051	3.908	11.311
M05	–	-0.147	-0.077	5.841	11.009
XSL	–	-0.158	0.007	6.793	19.967
E-MILES	–	-0.081	-0.011	3.369	16.151
CB07	–	-0.028	-0.034	3.462	8.453
RGB[a]	(I-K)=2.01	-0.124	-0.014	20.466	12.771
	(I-K)=2.54	-0.144	-0.043	22.407	22.139
	(I-K)=3.41	-0.143	-0.031	23.838	30.149
O-rich TP-AGB[a]	(I-K)=2.11	-0.304	-0.030	22.849	28.061
	(I-K)=3.19	-0.378	-0.112	23.624	47.078
	(I-K)=4.88	-0.690	-0.105	–	–
O-rich TP-AGB[b]	bin1	-0.281	-0.061	–	–
	bin5	-0.370	-0.010	–	–
C-rich TP-AGB[a]	(I-K)=2.61	-0.218	-0.549	43.837	228.035
	(I-K)=3.65	-0.408	-0.498	72.194	257.859
	(I-K)=4.46	-0.491	-0.358	–	–
C-rich TP-AGB[b]	bin1	-0.338	-0.385	–	–
	bin3	-0.299	-0.309	–	–

The [a] represents the average spectra of cool giants binned by broad-band colour (in Vega system) from the XSL simple stellar population models[35], while [b] are binned O- and C-rich spectra, observed by Lançon & Wood[13], and Lançon & Mouhcine[14], respectively. Each feature of star spectra is measured after smoothing and rebinning to match the PRISM resolution around the feature position.

Extended Data Table 2 | Stellar population properties of D36123 modeled based on XSL, E-MILES and CB07

Rest-frame	Property	XSL	E-MILES	CB07
	Redshift	$1.084^{+0.001}_{-0.001}$	$1.083^{+0.001}_{-0.001}$	$1.080^{+0.001}_{-0.001}$
	$M_*[\times 10^{10} M_\odot]$	$1.866^{+0.022}_{-0.022}$	$2.065^{+0.029}_{-0.038}$	$1.119^{+0.009}_{-0.008}$
	age [Gyr]	$1.556^{+0.047}_{-0.114}$	$1.934^{+0.026}_{-0.024}$	$0.991^{+0.001}_{-0.001}$
full	$Z/Z_\odot$	$1.319^{+0.041}_{-0.034}$	$0.506^{+0.011}_{-0.012}$	$0.975^{+0.004}_{-0.003}$
(0.3–2μm)	Av	$0.052^{+0.023}_{-0.024}$	$0.000^{+0.003}_{-0.000}$	$0.975^{+0.004}_{-0.003}$
	τ [Gyr]	$0.159^{+0.034}_{-0.031}$	$0.385^{+0.023}_{-0.027}$	$0.007^{+0.028}_{-0.007}$
	$SFR_{best}[M_\odot yr^{-1}]$	$0.073^{+0.045}_{-0.047}$	$0.460^{+0.023}_{-0.023}$	$0.000^{+0.003}_{-0.000}$
	SFR_{best}/SFR_{peak}	$0.001^{+0.003}_{-0.003}$	$0.090^{+0.033}_{-0.028}$	~ 0
	χ^2_R	55.5	46.1	117.0

Measurements and errors are as in Table 1.